ORIGINAL PAPER

Design, modeling and control of a hybrid grid-connected photovoltaic-wind system for the region of Adrar, Algeria

Y. Kebbati[1,2] · L. Baghli[3]

Abstract

The use of fossil energy for electricity production is an evident source of pollution, global warming and climate change. Consequently, researchers have been working to shift toward sustainable and clean energy by exploiting renewable an environmentally friendly resources such as wind and solar energies. On the other hand, energy security can only be achieved by considering multiple resources. Large-scale renewable energy power plants are a key solution for diversifying the total energy mix and ensuring energy security. This paper presents a contribution to diversify the energy mix in Algeria and help mitigate power shortages and improve grid performance. In particular, the paper aims at designing and modeling a large-scale hybrid photovoltaic-wind system that is grid connected. An innovative control approach using improved particle swarm optimized PI controllers is proposed to control the hybrid system and generate the maximum power from the available wind and solar energy resources. Furthermore, economic, environmental and feasibility studies of the project were conducted using HOMER software to assess the viability of the system and its contribution to reduce greenhouse gas emissions.

Keywords Renewable energy systems · Photovoltaic · Particle swarm optimization · Wind turbine · Adaptive control

Introduction

In today's world with an ever-increasing energy demand due to the developing industry and modern lifestyle, fossil fuel resources are being overexploited. Such high consumption rates caused a significant surge in greenhouse gas (GHG) emissions which effectively lead to a rise in earth's temperature. The side effects of global warming are nowadays expressed more than ever leading to droughts, extreme weather, flooding, etc. In addition, reserves of oil and natural gas are being rapidly depleted. Dependance on fossil fuel has become a serious issue that needs urgent attention on any levels. For instance, the economic sector in Algeria relies

✉ Y. Kebbati
  yassine.kebbati@univ-evry.fr

1 Department of Energy Engineering, Institute of Water and Energy Sciences (Incl. Climate Change), PAN African University, Tlemcen, Algeria

2 Department of Electrical and Electronics Engineering, Paris Saclay University, Evry, France

3 GREEN-ENSEM, University of Lorraine, Nancy, France

mainly on hydrocarbons exportation. The country's daily production reaches 92.1 billion cubic meters of natural gas in addition to 1.54 million barrels of crude oil. This huge reliance on fossil fuels has a major effect on the economy of the country as the prices of oil and gas are rarely stable. Oil and gas exports account for nearly 20% of the gross domestic product and about 85% of total exports (Mustapha et al. 2018). Over the last years, the fall of oil prices has widely affected the economy resulting in a huge deficit in the country's budget. Between 2014 and 2016, the price of one barrel of oil fell from $100 to $45.13 leading to a reduction of the total revenues by two thirds, dropping from $60 billion in 2014 to less than $20 billion in 2016. With this sharp decline, the country's gross domestic product (GDP) fell from $235 billion in 2014 to $160 billion in 2016. Moreover, fossil fuel prices dropped recently due to the COVID-19 pandemic and the global economic recession (Yoshino et al. 2021). In 2015 for instance, the state's budget reached its lowest record at − 15.3% of the total GDP.

Electricity and oil prices are majorly subsidized in Algeria. For instance, electricity costs 0.04 $/kWh which is among the lowest prices in the world (GlobalPetrolPrices.com 2020). However, since the emergence of the oil crisis, the subsidies started decreasing, and fossil fuel prices are

now growing more and more expensive. Subsidized electricity prices lead to one of the most irrational consumptions in the continent. The latter reached 1302 kWh per capita in 2020 and it is expected to exceed 150 TWh in 2030 (Index Mundi 2021). In light of the projection studies and as fossil fuel resources are none renewable and unsustainable, Algeria's oil reserves are expected to only last for the next 50 years. Similarly, natural gas is expected to cover the next 70 years (Harrouz et al. 2017). The major dependance on fossil fuels and the irrational power consumption in Algeria results in considerable amounts of GHG emissions. Over the last decades, significant levels of GHG emissions have been reached, which causes an impactful deterioration of the ecological system increasing global warming and further accelerating climate change. There is no doubt that the shift toward renewable energy resources is a more ecological and sustainable choice. Thus, integrating renewable energies will reduce fossil energy dependency and dramatically decrease GHG emissions. Consequently, researchers have been working to further develop renewable energy systems in order to increase their efficiency and extract the maximum possible energy from renewable resources.The goal is to become independent of fossil fuel resources and cover 100% of power demand from renewable energies. For instance, (Podder et al. 2019) reviewed the maximum power point tracking techniques according to their 8 categories to increase the efficiency of photovoltaic systems. (Wijeratne et al. 2019) investigated the current approaches for the design and development of distributed solar PV systems and their efficacy. (Dhimish and Alrashidi 2020) analyzed the effect of cold weather conditions on the efficiency of PV systems over the years, and their studies were based on the weather patterns in UK and in Australia. (Singh et al. 2021) provided a solution to increase the performance of wind turbine systems while reducing their overall cost. Their approach relies on minimizing the operating temperature of generator windings and bearings which reduces overheating of the system. (Kumar et al. 2021) carried out a technical review on the methods and techniques for damage detection in wind turbine systems using several signal processing methods. To enhance heat absorption from solar energy, (Serradj et al. 2021) conducted a study to use passive baffles in an attempt to improve the yield of single-slope solar still. The latter is useful in water desalination applications. (Genç 2011) compared the economic viability of wind turbine and diesel water pumping systems in five different regions in Turkey; the authors explored various energy conversion systems to evaluate wind power and the amount of water to be pumped. (Gökçek and Genç 2009) used the levelized cost of electricity to evaluate the effect of different wind energy conversion systems on the final wind energy cost. Similarly, (Fadlallah et al. 2021) used a strategic perspective to explore the viability of wind energy systems in Sudan. The authors used

HOMER software to identify the optimal wind system and best locations for wind farm installation over 21 different sites. (Genç et al. 2021) provided a method to determine the most appropriate site for wind power systems. Their approach was based on geographic information combined with multi-criteria decision making that takes into account several factors like wind potential, roads and water sources. The same approach was used in (Genç et al. 2021) for site selection in the coastal line of turkey for offshore wind farms installations. Similarly (Shata et al. 2006) analyzed wind data for the Mediterranean see in Egypt to determine wind characteristics for assessing the viability of electricity generation using wind turbines.

Worldwide energy consumption in 2012 had a respectable share of 19% from renewable sources; the contribution of renewable energy continued to rise year after year reaching 19.3% in 2015, of which 1.6% goes to solar, wind, biomass and geothermal power combined (Corry et al. 2016). Algeria is home to one of the world's greatest solar deposits; the duration of sun exposure is more than 2000 h a year, up to 3900 h in the highlands and the desert. This means that the country enjoys from 1700 to 2,263 kWh/m^2/year of solar energy (Maoued et al. 2015). The south of Algeria has significant wind resources, especially the region of Adrar, where average wind speeds range from 4 to 6 m/s, which makes it very attractive for the deployment of wind farms (Maoued et al. 2015). Figure 1 shows the annual distribution of mean wind speed in Algeria at 10 m altitude and the average daily solar irradiation (Boudia et al. 2016).

The Algerian government is trying to attract investments in wind and solar energies by establishing suitable policies to install 5 GW of wind power and 13.6 GW of solar PV by 2030. Moreover, the country launched in 2011 an ambitious renewable energy and energy efficiency program with the vision of developing and diversifying renewable energy resources. The goal of the program is to install 22 GW by 2030, of which 10 GW is aimed to be exported to the European market and 12 GW is dedicated to the national market (Abada and Bouharkat 2018). The distribution and share of renewable energy technologies are shown in Fig. 2.

Algeria is known for its important potential in hydrocarbon resources, but it also houses a huge solar energy potential (Kabir et al. 2018; Bouraiou et al. 2020) thanks to its location in the Mediterranean basin. The southern part of the country receives more sunshine as it lies exactly in the sunbelt. Wind energy is the second most abundant resource; half of the country's surface shows a considerable average wind speed that favors wind energy exploitation (Nedjari et al. 2018; HIMRI et al. 2020). Judging by the available resources, the integration of solar photovoltaic (PV) and wind energy systems is a key solution to further diversify the energy mix in the country and increase energy security. Grid-connected PV systems have proven
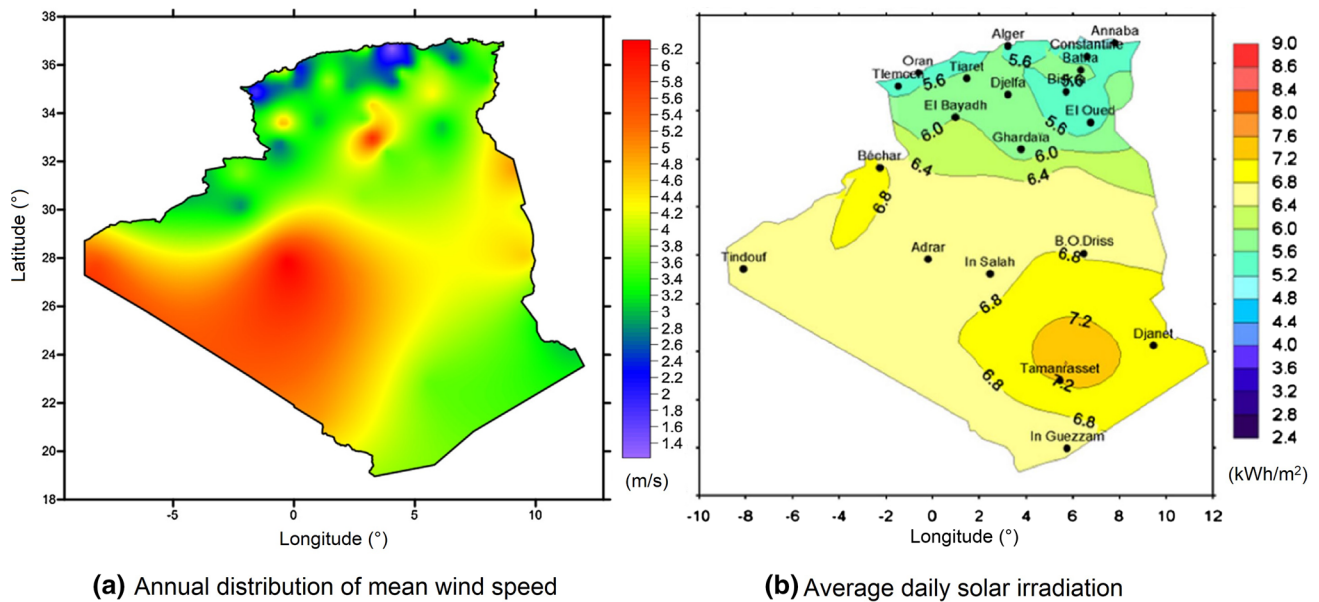
(a) Annual distribution of mean wind speed

(b) Average daily solar irradiation

Fig. 1 Mean wind speed and average solar irradiation in Algeria (Boudia et al. 2016)

Share of renewable energies %

- Photovoltaic Solar
- Wind Power
- Solar Thermal
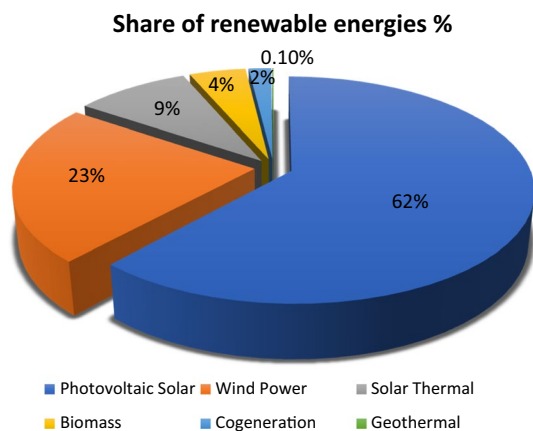- Biomass
- Cogeneration
- Geothermal

Fig. 2 Share of renewable energy technologies in energy efficiency program

their potential and capacity to provide adequate energy to the grid, and these systems have been studied in (Kidar et al. 2021) and (Zerglaine et al. 2021). In highly distributed populations, extending power grids may become too expensive. For instance, (Terfa et al. 2022) proposed the use of distributed micro-power plants as a solution to the expensive grid extension. On the other hand, the southwest region is very suitable for wind energy systems which have been studied in (WANG et al. 2018) and (Charrouf et al. 2018). Furthermore, (Dekali et al. 2021) worked on the design, modeling and experimental build of a 1.5 kW low-cost wind energy conversion system based on current-controlled DC motors and tip speed ratio (TSR) based on maximum power point tracking (MPPT).

Adrar represents the second largest province in Algeria, situated in the heart of the desert with an area of 427,368 km^2. Due to its considerable wind and solar energy potential, it has been selected as the case study. The district of Adrar is precisely situated at 27.52° north of latitude and 0.17° west of longitude occupying 663 km^2 of the whole province. Around 65,000 inhabitants live mainly in the city of Adrar, even though the province is vast. The climate in Adrar is a Saharan arid one. As for the topography, Adrar is characterized by a relatively flat terrain with the highest point reaching 421 m. The location of the case study region is given in Fig. 3. Renewable energy resources vary in nature, solar and wind proved to be intermittent and this fact makes them a bit tricky to harness, because their intermittency creates challenges to maintaining a continuous and reliable power supply. In grid-connected systems, it is even more difficult especially in the case of weak grids that are not able to handle the fluctuation of power generation when the amount of integration of solar or wind is important. Hybrid systems can tackle this issue, combining solar PV with wind is an attractive solution that provides reliable and economical renewable power generation.

In this article, a hybrid grid-connected PV-wind system is designed, modeled and controlled with optimized PI controllers. A new improved particle swarm optimization (PSO) algorithm was developed to optimize the gains of the PI controller. The proposed system was assessed for two critical months of the year to evaluate its contribution to grid performance. Hourly weather data averaged over the last

Fig. 3 Location of Adrar on the map

10 years have been used to simulate the system. Finally, the economic and environmental analysis of the system was carried out using Homer software.

Materials and methods

Site selection and resource assessment

The province of Adrar has been selected for this study thanks to its potential in both wind and solar energies; it is situated in the heart of the Algerian desert located at 27.52° N and 0.17° W. The district occupies 663 km² and has a population of about 65,000 inhabitants (Djamai

et al. 2011). The climate in the province is a Saharan arid one with a topography characterized by flat terrain reaching the highest point of 421 m. Based on hourly global irradiation data on a horizontal surface, the province of Adrar receives average daily irradiation of up to 5.7 kWh/m²/day. During the winter season, the global radiation drops in between 3 and 4 kWh/m²/day. The highest potential solar radiation is observed from March to October, with average global radiation varying between 5.5 and 7.5 kWh/m²/day (Bouzidi B. 2011). The Algerian government aims to generate 27% of its energy from renewables by 2030, and six grid-connected solar power plants have already been commissioned reaching a total capacity of 91 MW (Yaneva. M. 2016). The province of Adrar is also

favorable for wind energy systems. Wind speed distributions show that 20% of wind speeds are 4 m/s or less, 62.5% are between 5 and 9 m/s, while the rest are above 10 m/s according to the wind atlas (Atlas Climatologique National. 2008). The latter states that average speeds are the lowest from 8 pm to 5 am. The maximum speeds are reached in the morning around 10 am, and medium speeds are maintained throughout the day. The region of Adrar is characterized by a hot and very arid Saharan climate, cold nights in winter, scarce rainfall and seasonal sandstorms. The hottest month is July where the mean minimum and maximum temperatures are 26.8 °C and 44.9 °C, respectively. January marks the coldest month with 4.5 °C and 20.3 °C as the respective mean minimum and maximum temperatures (Atlas Climatologique National. 2008). Table 1 shows average horizontal global irradiation, average maximum temperatures and humidity levels on a monthly basis (Dabou et al. 2016).

Table 1 Monthly average of daily weather parameters in 2014 (Dabou et al. 2016)

Months	H (kW h/m^2)	T$_{max}$ (C°)	RH (%)
January	4.36	22.67	38
February	5.49	26.06	26
March	6.64	27.98	21
April	7.73	32.72	14
May	7.8	39.76	12
Jun	8.1	42.42	11
July	7.48	47.39	8
August	6.96	45.86	13
September	6.16	43.93	15
October	5.48	37.15	18
November	4.23	27.28	35
December	4.26	20.68	43
Mean Monthly	6.22	34.49	21.16

Fig. 4 Monthly average direct normal and global horizontal irradiation
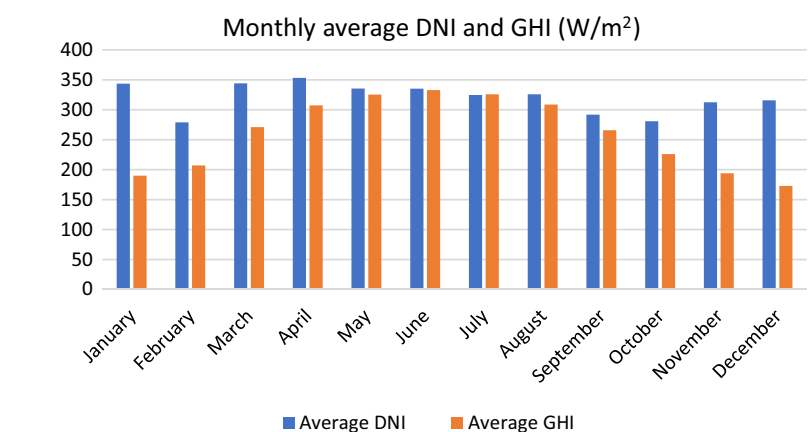
Weather data of Adrar

Data of solar irradiation, wind speed and temperature were extracted from a weather file generated using METEONORM 7.1. The data are in an hourly form and covers many parameters. The data cover an average of the ten last years up to 2021. Relevant data are converted into a monthly basis and are represented in Figs 4, 5, 6.

The figures show high average direct normal irradiation (DNI) content, especially in winter and spring, and the software indicates an error of 10%. The DNI levels tend to decrease in February and October. The monthly average direct horizontal irradiation (DHI) and global horizontal irradiation (GHI) levels follow a similar trend where the highest levels are recoded during the summer season, especially June and July. Average monthly wind speed reaches its maximum of around 6 m/s in May, and the maximum speed is around 16 m/s, which is very suitable for wind energy systems considering wind turbines with high hub heights. Overall, summer and spring seasons receive most of the wind energy potential. The trend
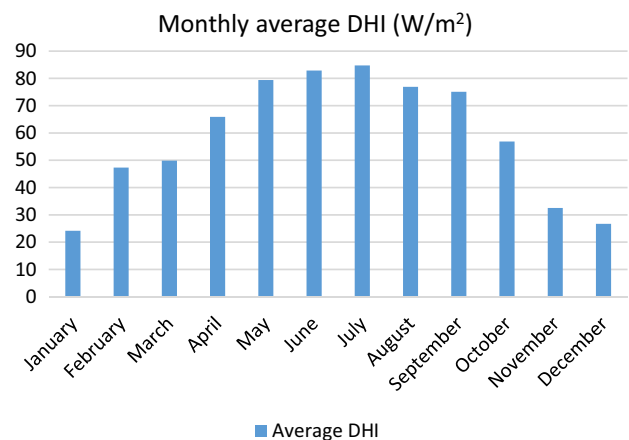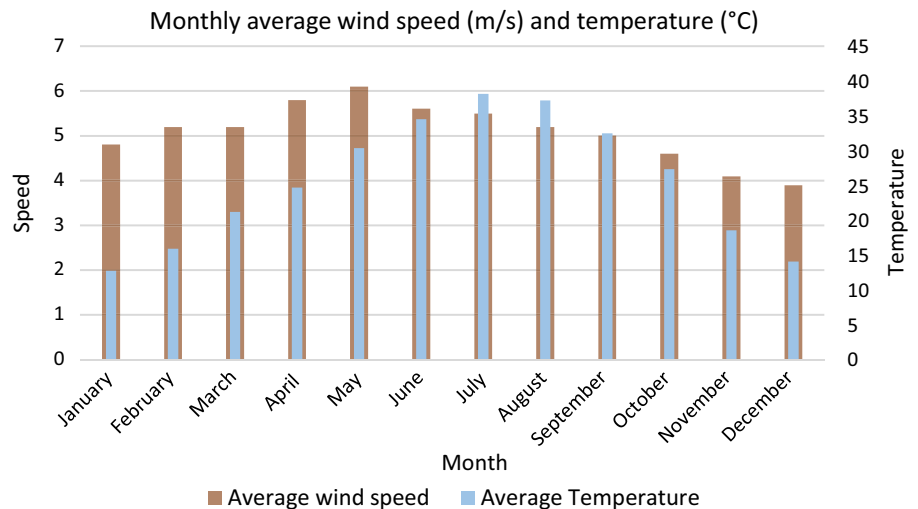

Fig. 5 Monthly average diffuse horizontal irradiation

Fig. 6 Monthly average wind speed and temperature

Monthly average wind speed (m/s) and temperature (°C)

for average temperature shows a noticeable increase during summer, and the peak is recorded in July with and average value of 37 °C. This would decrease the efficiency of PV generators, but for the other seasons, it is much cooler and more favorable. The software indicates a temperature error of 0.3 °C.

Load profile of Adrar

The load profile of Adrar covers the amount of power consumed by the different sectors in the town. Daily data were used to determine the peak demand in the region. For representing the load, hourly power production data of the Adrar's central power plant were used instead, due to its availability. It is worth mentioning that the central power plant not only supplies the entire commune of Adrar, but part of its production goes to the neighboring cities as well. Figure 7 depicts the monthly average power produced from the central power plant.

The peak demand occurs during summer, and this is justified by the cooling load since the place has a Saharan climate and temperatures skyrocket during this period. Although consumption rates in August are the highest, the peak demand for 2017 occurred in June reaching 63 MW, and this represents an increase of about 6.5% compared to 2016. Based on the observed data, August and January are selected for simulation analysis in this study. August represents the summer period where the peak loads appear accompanied by high temperatures, while January represents the winter period where the wind energy potential and the load are the lowest. The choice of these two months aims to simulate the designed system for two extreme cases to be able to evaluate its contribution to power production.
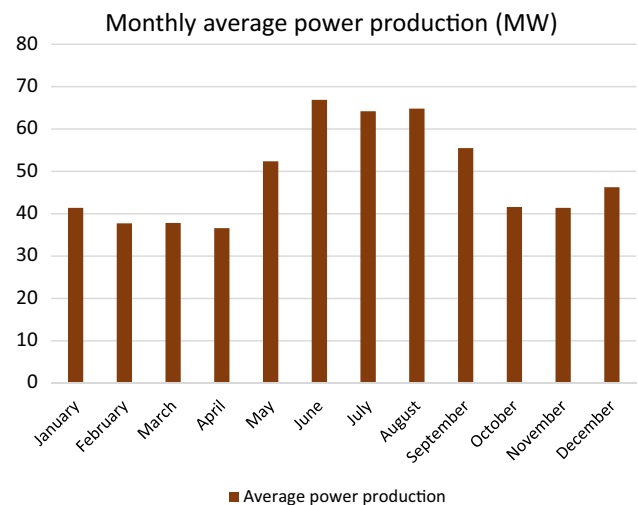

Monthly average power production (MW)

Fig. 7 Monthly average power output of Adrar central power plant

System design and sizing

The sizing of the system is based on the production capacity and the energy potential of Adrar, while the design addresses the performance and capital cost of the overall system. Thus, the system is sized to meet at least half of the peak demand in Adrar, opting for a higher capacity is not viable since the capital cost will be too high and a vast area will be required. This has so many drawbacks, for instance, it will be too cumbersome to clean PV panels from dust depositions. In addition, the design employs certain topologies to maximize power output, minimize losses and reduce the upfront investment needed.

PV system

The PV generator produces 5 MW and consists of 14,320 panels, with each panel having a rated power of 350 watts. To provide higher power levels, the multi-string inverter topology has been adopted. Each DC-DC boost converter is linked to an inverter, while connecting five PV panel sets in parallel. Each PV panel set contains eight panels in series. The whole PV system contains 358 inverters, 358 boost converters and a total of 14,320 panels distributed over the 358 strings. To minimize the surface needed for panels, the two sets of each string face southward with a spacing distance of three meters between the panels to avoid shading. The strings are then placed side by side as shown in Fig. 8, with this configuration the area is minimized to about 0.064 km^2. Based on the latitude of Adrar ($25° < \emptyset = 27.52° < 50°$) and according to (SolarPanelTilt.com 2021), the optimal tilt angle for the PV panels is obtained as: ($\beta = 0.76 \times \emptyset + 3.1 = 25°$).

Wind system

The wind farm consists of 10 large wind turbines; each one has a rated power of 3 MW. Adrar is a region of pressure difference close to the Atlantic Ocean where the wind blows from the west. Thus, the wind turbines face westward. The general rule-of-thumb for wind farm spacing speculates a spacing distance of about five to seven rotor diameters between two turbines (Meyers et al. 2012). Hence, to avoid turbulence and ensure maximum power extraction, a spacing distance of 450 m is maintained between the turbines. The 10 turbines are divided into three sets. The first set comprises four aligned turbines, while the other two sets contain three turbines each as shown in Fig. 9. The estimated surface required for the wind farm is about 1.8 km^2.

The wind generators are linked to medium voltage lines (10 kV), and a step-up transformer is required to match the output voltage with that of the medium voltage lines and allow grid connection. The total system has a rated power of 35 MW, but this is rarely maintained due to the fluctuations of irradiation levels and wind speeds. However, the system should undoubtedly improve the grid performance and eliminate power outages during peak demands.
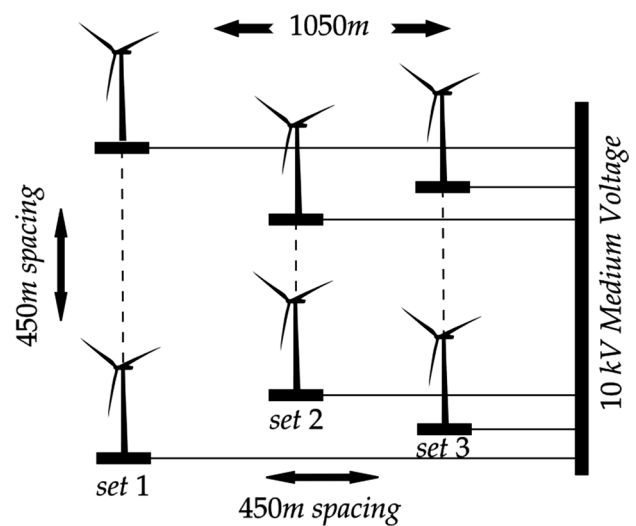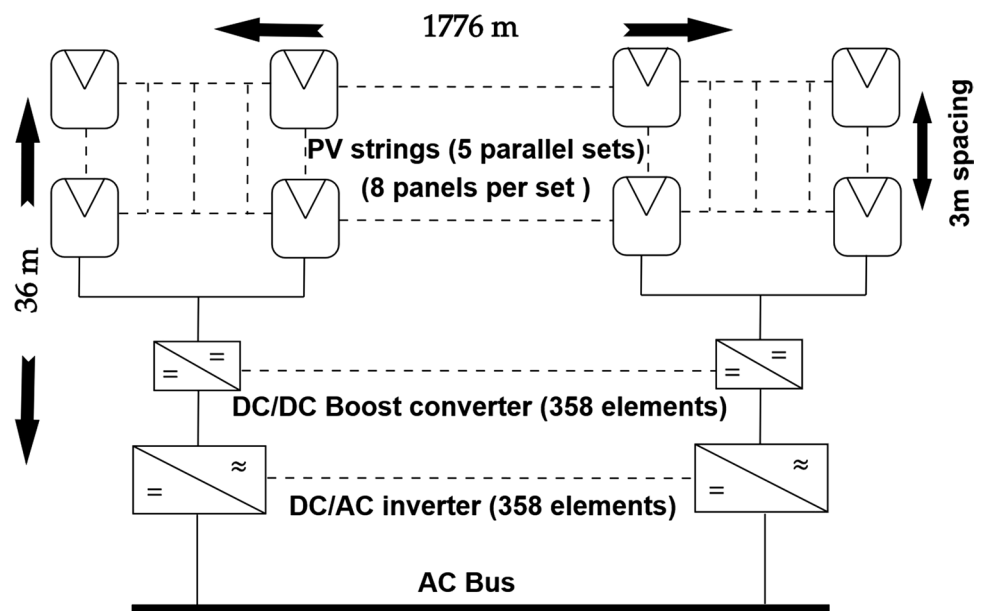

Fig. 9 Wind farm scheme

Fig. 8 PV plant scheme

Modeling of the PV system

PV generator

The PV array is modeled based on four equations that govern the output current:

Photocurrent : $\quad I_{ph} = \left[I_{sc} + k_i \cdot (T - T_n) \right] \cdot \dfrac{G}{1000}$ (1)

Saturation current: $\quad I_0 = I_{rs} \cdot \left(\dfrac{T}{T_n} \right)^3 \cdot$

$$\exp\left[\frac{q \cdot E_{g0} \cdot \left(\frac{1}{T_n} - \frac{1}{T} \right)}{n \cdot K} \right]$$ (2)

Reverse saturation current : $\quad I_{rs} = \dfrac{I_{sc}}{\exp\left(\frac{q \cdot V_{oc}}{n \cdot N_s \cdot K \cdot T} \right) - 1}$ (3)

Output current: $\quad I = I_{ph}$

$$- I_0 \cdot \left[\exp\left(q \cdot \frac{(V + I.R_s)}{n.K.N_s.T} \right) - 1 \right] - \frac{V + R_s.I}{R_p}$$ (4)

where I_{ph}, I_0, I_{rs} and I_{sc} are the respective photogenerated current, diode saturation current, reverse saturation current and short-circuit current. k_i, T, T_n, q and G are the current coefficient, the temperature, the nominal temperature, the electron charge and the irradiation, respectively. E_{g0}, K, N_s, R_s and R_p represent the semiconductor bandgap energy, the Boltzmann's constant, the number of cells connected in series and the equivalent series and parallel resistors, respectively. The monocrystalline Amerisolar AS-6 M PV panel was chosen due to its high efficiency of 18.04%, competitive price of 0.3 \$\kW and good performance in hot climates. Moreover, monocrystalline solar cells proved better performance in desert climates than other types of solar cells according to (Shaltout et al. 2000). The main panel specifications are given in Table 2 (see Appendix). The series (R_s) and shunt (R_p) resistances are calculated according to (Villalva et al. 2009).

Maximum power point control

To keep the PV generator working at maximum power, an MPPT tracker has been added to the model. Perturb and observe algorithm has been chosen, because of its precision, simplicity and ease of implementation. The algorithm is based on the introduction of perturbations to the voltage and the observation of power output change. The signs of

Table 2 Main characteristics of the AS-6 M module

I_{sc}	Short-circuit current (A)	9.68
k_i	Short-circuit current of the cell at 25 °C and 1000 w/m^2	5×10^{-4}
q	Electron charge (C)	1.6×10^{-19}
V_{oc}	Open-circuit voltage (V)	46.5
n	The ideality factor of the diode	1.2
K	Boltzmann's constant (J/K)	1.38×10^{-23}
E_{g0}	Bandgap energy of the semiconductor (eV)	1.12
N_s	Number of cells connected in series	72
R_s	Series resistor (Ω)	0.100
R_p	Shunt resistor (Ω)	515
P_{max}	Maximum output power(W)	350
V_{mpp}	Maximum power voltage(V)	37.9
I_{mpp}	Maximum power current(A)	9.24

the last perturbation and the last power increment are used to decide the next perturbation; this continuous loop keeps the output power at its maximum. The output voltage of the array is injected directly into a DC-DC converter. Figure 10 shows the MPPT algorithm.

DC-DC converter

The DC boost converter has high efficiency and robustness, and it is capable of stepping up the output. The converter receives the fluctuating DC output voltage of the PV array and converts it into a fixed stepped-up DC voltage. The equivalent electrical circuit is shown in Fig. 11, and Eqs. (5,6) are used for modeling.

Loop 1 : $\quad L \dfrac{di_L}{dt} = V_e - V_c(1 - \alpha)$ (5)

Loop 2 : $\quad C \dfrac{dV_c}{dt} = i_L(1 - \alpha) - \dfrac{V_c}{R}$ (6)

where a represents the duty cycle obtained from the MPPT and used to generate the pulse width modulation (PWM) signal which then controls the opening and closing of the switch (represented by K_2 in the circuit).

Three-phase inverter

The connection of the PV system to the AC bus is done via a voltage source inverter. The output of the boost converter is a fixed DC voltage; it is fed into a grid-tied three-phase inverter. Such inverters are used only in high power applications, and their output is a three-phase voltage (v_a, v_b and v_c), and the latter is controlled by PWM signals. Pulse width modulation is the process of changing the width of a pulse

Fig. 10 MPPT algorithm
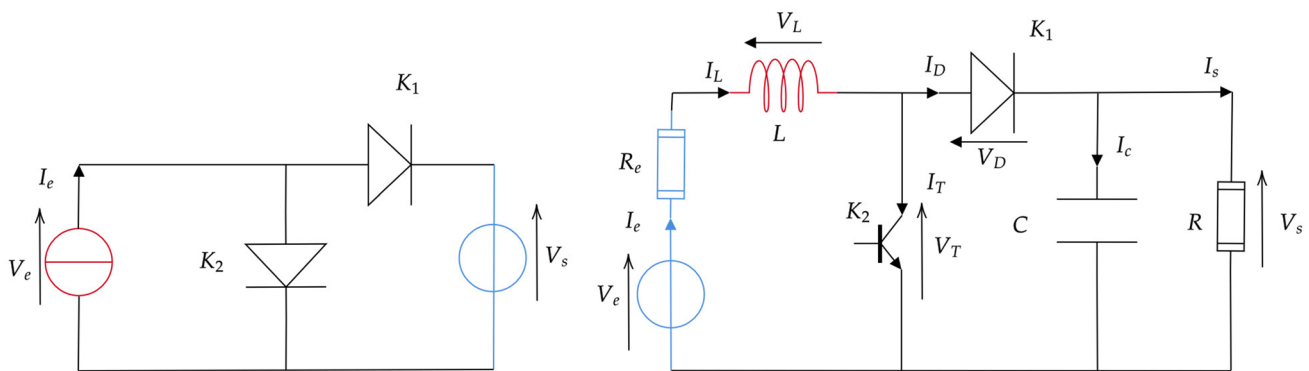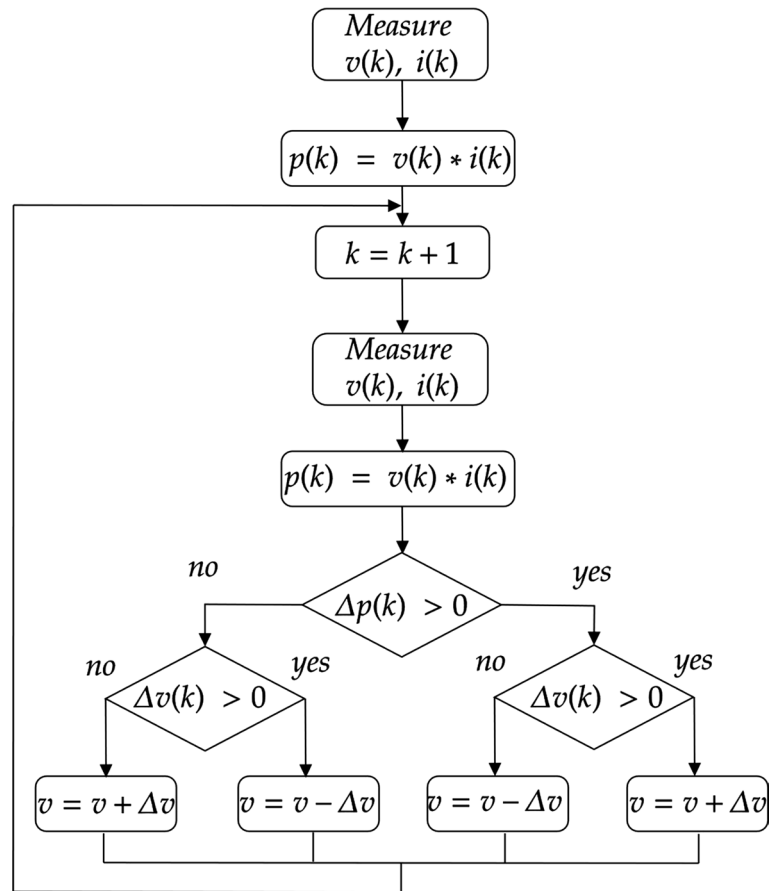
Fig. 11 DC-DC boost converter

train in direct proportion to a small control signal. The electric circuit of the inverter with RL filter is shown in Fig. 12.

Three-phase inverters can be controlled in three types of frames, the synchronous rotating frame (d-q), the stationary reference frame (α-β) and the natural frame (a-b-c). In d-q frame control, three-phase voltages and currents are transformed by Park's transformation into the d-q reference frame that rotates synchronously with the grid voltage. Thus, three-phase variables become DC quantities. As the control variables are DC, different filtering methods can be used. In addition, an innovative PSO-PI, which will be detailed, is designed to achieve good performance in this reference frame control. The model of the inverter is determined by Eqs. (7–9) (Isen et al. 2016):

$$\text{a} - \text{b} - \text{c} \quad V_{k0} = L\frac{di_k}{dt} + Ri_k + V_{gk} + V_{n0} \tag{7}$$

Fig. 12 Equivalent electric circuit of the three-phase inverter
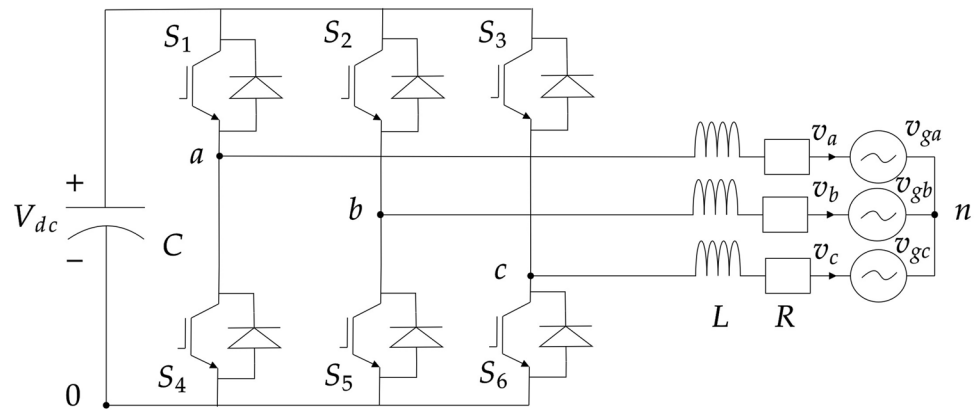
$$V_{n0} = \frac{1}{3}\left(V_{a0} + V_{b0} + V_{c0}\right) \tag{8}$$

$$V_{k0} = S_k V_{dc} = \begin{cases} V_{dc}\ S_k = 1 \\ 0\ S_k = 0 \end{cases} \tag{9}$$

where k, S and R represent the phase of the inverter, the state of upper switches and the filter series resistor, respectively. L and V_n are the filter inductance and the voltage difference between grid neutral point and negative V_{dc}. In each phase of the inverter, the two switches are supposed perfect and work simultaneously, and this allows us to write Eq. (10). Considering the voltages between a, b, c and the ground, we can express the model of the inverter by Eq. (11) (Mourad 2016):

$$\begin{bmatrix} v_{a0} \\ v_{b0} \\ v_{c0} \end{bmatrix} = \frac{V_{dc}}{2} \times \begin{bmatrix} S_a \\ S_b \\ S_c \end{bmatrix} \tag{10}$$

$$\begin{bmatrix} v_a \\ v_b \\ v_c \end{bmatrix} = \frac{1}{3} \times \begin{bmatrix} 2 & -1 & -1 \\ -1 & 2 & -1 \\ -1 & -1 & 2 \end{bmatrix} \times \frac{V_{dc}}{2} \times \begin{bmatrix} S_a \\ S_b \\ S_c \end{bmatrix} \tag{11}$$

To control the inverter, the grid voltages are measured and used to determine the grid angle θ by means of phase lock loop (PLL). (Isen et al. 2016) explain the PLL method in detail. The grid angle is then used in Park's transformation to transform the grid voltages (V_{ga}, V_{gb} and V_{gc}) from a-b-c reference frame to d-q frame which simplifies the control, and the result is V_{gd} and V_{gq} (the d-q components of the grid voltages). Following the same transformation method, V_{id} and V_{iq} (the d-q inverter components) are generated from the output voltages of the inverter. Park's transformation is given as (Isen et al. 2016):

$$\begin{bmatrix} V_d \\ V_q \end{bmatrix} = \frac{2}{3} \begin{bmatrix} \cos\theta & \cos\left(\theta - \frac{2\pi}{3}\right) & \cos\left(\theta - \frac{4\pi}{3}\right) \\ -\sin\theta & -\sin\left(\theta - \frac{2\pi}{3}\right) & -\sin\left(\theta - \frac{4\pi}{3}\right) \end{bmatrix} \begin{bmatrix} V_a \\ V_b \\ V_c \end{bmatrix} \tag{12}$$

RL filter

The d-q voltage components of both the inverter and the grid are used in a vector control mechanism implemented within an RL filter to generate active (P) and reactive (Q) powers. The RL filter model is based on the following equations (Gaillard. A. 2010):

$$a - b - c: \quad V_a = -R_f.i_a - L_f\frac{di_a}{dt} + V_{ga} \tag{13}$$

$$V_b = -R_f.i_b - L_f\frac{di_b}{dt} + V_{gb} \tag{14}$$

$$V_c = -R_f.i_c - L_f\frac{di_c}{dt} + V_{gc} \tag{15}$$

$$d - q \quad V_d = -R_f.i_d - L_f\frac{di_d}{dt} + L_f\omega i_q + V_{gd} \tag{16}$$

$$V_q = -R_f.i_q - L_f\frac{di_q}{dt} - L_f\omega i_d + V_{gq} \tag{17}$$

where

- L_f represents the inductance of the filter.
- R_f is the resistor of the filter.

The RL filter connects the inverter to the grid because they have different voltage amplitudes and different phases, and the filter maintains a voltage difference between the grid and the inverter which allows power to flow toward the grid. In addition, it reduces the harmonics that are generated by the electronic components of the system. The measured active and reactive powers are then directly compared to reference values (P*) and (Q*), Q* is always set to zero to eliminate reactive power generation, and this ensures zero phase angle between voltage and current leading to unity

power factor. On the other hand, P* is set based on the output of the PV generator. The resulting errors are regulated by the PSO-PI controller and yield reference d-q inverter voltages (V_d* and V_q*). The control mechanism responsible for finding (V_d* and V_q*) is shown in Fig. 13:

With the help of Park's inverse transformation, the obtained voltages are transformed back into three-phase reference inverter voltages (V_a*, V_b* and V_c*) to be compared with a repetitive MATLAB sequence which in turn generates PWM signals that control the switches of the inverter. The PWM signals represent the state of the upper switches given in Eq. (9). Park's inverse transformation, known as d-q to a-b-c transformation, is given by the following equation (Isen et al. 2016):

$$\begin{bmatrix} V_a \\ V_b \\ V_c \end{bmatrix} = \begin{bmatrix} \cos(\theta) & -\sin(\theta) \\ \cos\left(\theta - \frac{2\pi}{3}\right) & -\sin\left(\theta - \frac{2\pi}{3}\right) \\ \cos\left(\theta - \frac{4\pi}{3}\right) & -\sin\left(\theta - \frac{4\pi}{3}\right) \end{bmatrix} \begin{bmatrix} V_d \\ V_q \end{bmatrix} \tag{18}$$

Modeling of the wind system

The wind farm consists of a set of wind turbines, which are divided into dynamic and mechanical models, in addition to the electrical model of a doubly fed induction generator (DFIG) linked to the turbine via a gearbox. The stator of the DFIG is directly connected to and synchronized with the grid, while the connection of the rotor is ensured by a back-to-back converter consisting of a rectifier, an inverter, a DC bus and an RL filter as seen in Fig. 14.

Dynamic model of the wind turbine

The mechanical power extracted from wind is characterized by Eq. (19):

$$P_t = \frac{1}{2}\rho Cp(\lambda, \beta)\pi R^2 V^3 \tag{19}$$

with the TSR defined as:

$$\lambda = \frac{\Omega_t . R}{V} \tag{20}$$

The parameters ρ, Cp and R are the air density, the power coefficient and the turbine blade radius, respectively. V, Ω_t and β are the respective wind velocity, rotational speed and pitch angle of the turbine. The maximum power coefficient is a function of λ and β. According to (Gaillard. A. 2010), the maximum power coefficient for a 3-MW wind turbine is given by:

$$C_p = C_1 \times \left(C_2 \times \frac{1}{\lambda_i} - C_3 \times \beta - C_4\right) \times \exp\left(-\frac{C_5}{\lambda_i}\right) + C_6 \times \lambda \tag{21}$$

where $\left(\frac{1}{\lambda_i} = \frac{1}{\lambda + 0.08 \times \beta} - \frac{0.035}{\beta^3 + 1}\right)$ and the coefficients C_i are given in Table 3 (see Appendix).

Mechanical model of the turbine

The torque of the generator (T_m) and turbine (T_t) is used to evaluate the speed (Ω_m). The behavior of the mechanical system is governed by the classical rotational dynamics equation:
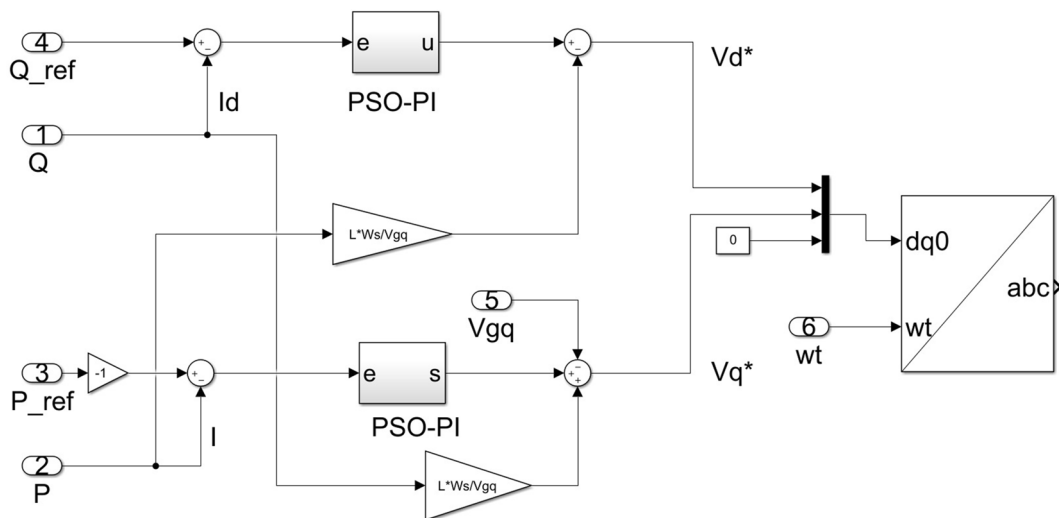

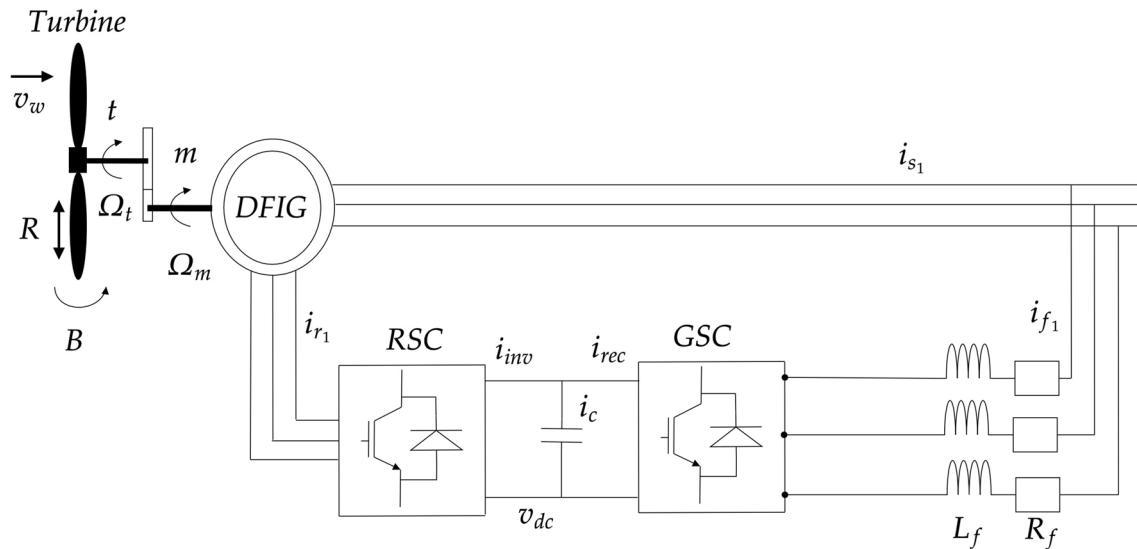**Fig. 13** Simulink model of the inverter control

Fig. 14 DFIG-based wind system

Table 3 Power coefficients

C_1	C_2	C_3	C_4	C_5	C_6
0.5176	116	0.4	5	21	0.0068

$$\left(\frac{J_t}{G^2} + J_m\right)\frac{d\Omega_m}{dt} + f_v \times \Omega_m = T_t - T_m \tag{22}$$

where J_t and J_m are the inertia moments of the turbine and the generator, and f_v is the friction coefficient of the generator.

MPPT control for the wind turbine

The MPPT technique relies on controlling the rotational speed of the generator to ensure maximum power extraction, and this is achieved by imposing a reference torque on the machine. Thus, the TSR must be maintained at its optimal value (λ_{opt}) to maintain the power coefficient at its maximum value C_{pmax} as well. The turbine control and the MPPT technique are demonstrated in Fig. 15.

Model of the doubly fed induction generator

The DFIG is modeled in Park's reference frame to facilitate the implementation of the vector control method. The model described in (Gaillard. A. 2010) is simplified where the fluxes are additive and the inductances are constant with a mutual sinusoidal variation between the rotor and stator windings as a function of the electrical angle θ_e and their axes. Equations (23–26) govern the stator and rotor voltages in the Park reference frame.

$$V_{sd} = R_s \cdot i_{sd} + \frac{d\varphi_{sd}}{dt} - \dot{\theta}_s \cdot \varphi_{sq} \tag{23}$$

$$V_{sq} = R_s \cdot i_{sq} + \frac{d\varphi_{sq}}{dt} + \dot{\theta}_s \cdot \varphi_{sd} \tag{24}$$

$$V_{rd} = R_r \cdot i_{rd} + \frac{d\varphi_{rd}}{dt} - \dot{\theta}_r \cdot \varphi_{rq} \tag{25}$$

$$V_{rq} = R_r \cdot i_{rq} + \frac{d\varphi_{rq}}{dt} - \dot{\theta}_r \cdot \varphi_{rd} \tag{26}$$

where V_{sd}, V_{sq} and V_{rd}, V_{rq} are the stator and rotor d-q voltages; i_{sd}, i_{sq} and i_{rd}, i_{rq} are the stator and rotor d-q currents. $\varphi_{sd}, \varphi_{sq}$ and $\varphi_{rd}, \varphi_{rq}$ are the stator and rotor d-q fluxes, R_r and R_s are the rotor and stator resistances, and θ_r and θ_s are rotor and stator angles. The stator and rotor flux d-q components are given by:
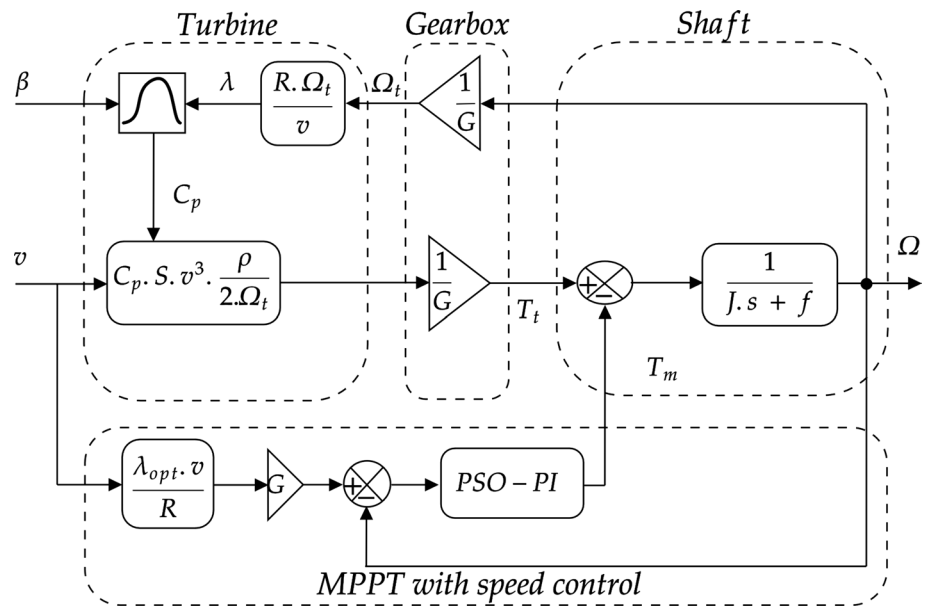
$$\varphi_{sd} = L_s.i_{sd} + m.L_m.i_{rd} \tag{27}$$

$$\varphi_{sq} = L_s.i_{sq} + m.L_m.i_{rq} \tag{28}$$

$$\varphi_{rd} = L_r.i_{rd} + m.L_m.i_{sd} \tag{29}$$

$$\varphi_{rq} = L_r.i_{rq} + m.L_m.i_{sq} \tag{30}$$

Fig. 15 Wind turbine with MPPT control mechanism

$$L_s = L_{fs} + L_m \tag{31}$$

$$L_r = L_{fr} + m^2 . L_m \tag{32}$$

where L_s, L_r and L_m are the stator/rotor cyclic inductances and the magnetizing inductance, respectively. L_{fs} and L_{fr} are the stator and rotor leakage inductances and m is the transformation ratio. Formulas (33–36) are used to calculate the stator and rotor active and reactive powers.

$$P_S = V_{sd} . i_{sd} + V_{sq} . i_{sq} \tag{33}$$

$$Q_s = V_{sq} . i_{sd} - V_{sd} . i_{sq} \tag{34}$$

$$P_r = V_{rd} . i_{rd} + V_{rq} . i_{rq} \tag{35}$$

$$Q_r = V_{rq} . i_{rd} - V_{rd} . i_{rq} \tag{36}$$

The electromagnetic torque T_m can be expressed in Eq. (37–38):

$$T_m = p . \left(\varphi_{sd} . i_{sq} - \varphi_{sq} . i_{sd} \right) \tag{37}$$

$$T_m = p . \frac{m . L_m}{L_s} . \left(\varphi_{sq} . i_{rd} - \varphi_{sd} . i_{rq} \right) \tag{38}$$

where p represents the number of pole pairs.

DFIG control

By neglecting the resistance of the stator windings, the simplified model of the DFIG in the d-q reference frame is obtained as the following:

$$V_{sd} = 0 \tag{39}$$

$$V_{sq} istance = U_s = \omega_s . \varphi_{sd} \tag{40}$$

$$V_{rd} = R_r . i_{rd} + \frac{d\varphi_{rd}}{dt} - \omega_r . \varphi_{rq} \tag{41}$$

$$V_{rq} = R_r . i_{rq} + \frac{d\varphi_{rq}}{dt} - \omega_r . \varphi_{rd} \tag{42}$$

The stator currents are obtained from the stator and rotor flux equations as:

$$i_{sd} = \frac{\varphi_{sd} - m . L_m . i_{rd}}{L_s} \tag{43}$$

$$i_{sq} = -m . \frac{L_m}{L_s} . i_{rq} \tag{44}$$

Thus, rotor flux equations become like the following:

$$\varphi_{rd} = \left(L_r - \frac{(m.L_m)^2}{L_s} \right).i_{rd} + m.\frac{L_m}{L_s}.\varphi_{sd} = \sigma.L_r.i_{rd} + m.\frac{L_m}{L_s}.\varphi_{sd} \tag{45}$$

$$\varphi_{rq} = L_r \cdot i_{rq} - \frac{(m.L_m)^2}{L_s} \cdot i_{rq} = \sigma \cdot L_r \cdot i_{rq} \tag{46}$$

With σ being the leakage coefficient:

$$\sigma = 1 - \frac{(m \cdot L_m)}{L_s \cdot L_r} \tag{47}$$

By replacing the direct and quadrature components of the rotor fluxes we obtain:

$$v_{rd} = R_r \cdot i_{rd} + \sigma \cdot L_r \frac{di_{rd}}{dt} + e_{rd} \tag{48}$$

$$v_{rq} = R_r.i_{rq} + \sigma.L_r \frac{di_{rq}}{dt} + e_{rq} + e_\varphi \tag{49}$$

where

$$e_{rd} = -\sigma.L_r.\omega_r.i_{rq} \tag{50}$$

$$e_{rq} = \sigma.L_r.\omega_r.i_{rd} \tag{51}$$

$$e_\varphi = \omega_r.m.\frac{L_m}{L_s}.\varphi_{sd} \tag{52}$$

The electromagnetic torque becomes as follows:

$$T_m = -p.\frac{m.L_m}{L_s}.\varphi_{sd}.i_{rq} \tag{53}$$

Hence, the active and reactive powers are given by Eqs. (54,55):

$$P_S = -v_{sq}.m.\frac{L_m}{L_s}.i_{rq} \tag{54}$$

$$Q_S = \frac{v_{sq}.\varphi_{sd}}{L_s} - v_{sq}.m.\frac{L_m}{L_s}.i_{rd} \tag{55}$$

From these expressions it is obvious that the choice of the d-q frame makes power produced from the stator proportional to the rotor q current component, while the reactive power is not proportional to the rotor d current component. This implies that independent control of the stator's active and reactive power is possible through the rotor d-q current components. For controlling the rotor d-q current components, reference d-q rotor currents are needed. These are obtained from the stator flux, which is estimated by the following formula:

$$\varphi_{sd-est} = L_s.i_{sd} + m.L_m.i_{rd} \tag{56}$$

The reference rotor current components are then generated as follows:

$$i_{rq}^* = -\frac{L_s}{p.m.L_m.\varphi_{sd-est}}.T_m^* \tag{57}$$

$$i_{rd}^* = \frac{\varphi_{sd-est}}{m.L_m} - \frac{L_s}{m.L_m.v_{sq}}.Q_s^* \tag{58}$$

Figure 16 shows the control mechanism of the DFIG, ensured by the rotor side converter (RSC).

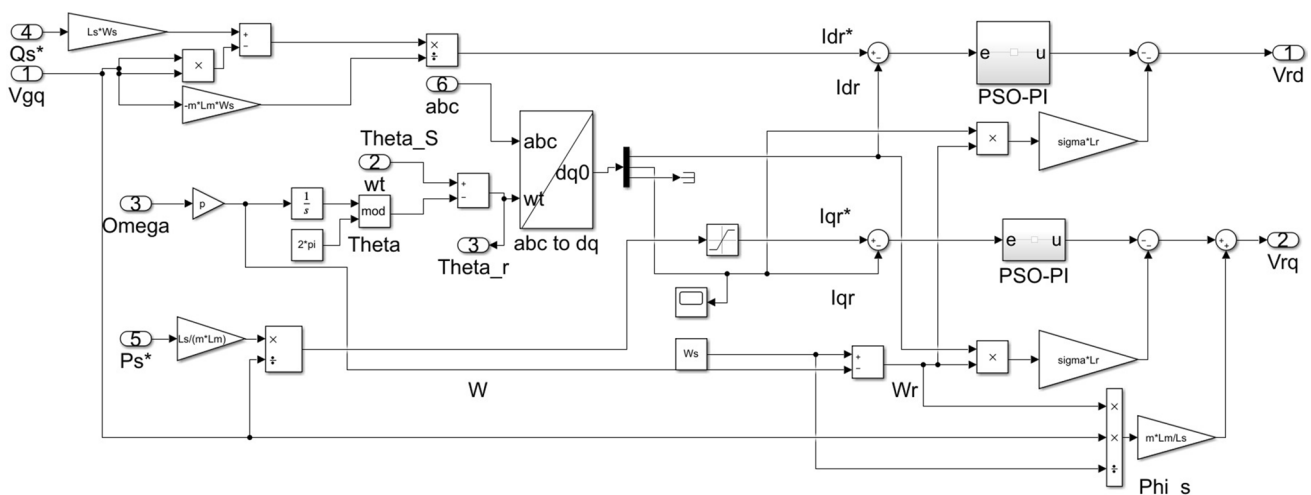The output voltages are then used to generate the PWM signal which controls the converter.

Fig. 16 Simulink model of the DFIG control

Filter and grid-side converter (GSC)

As shown in Fig. 17, the GSC is linked to the grid through an RL filter, and it allows the control of the DC bus voltage and the reactive power injected into the grid. Unity power factor is ensured by setting the reactive power to zero ($Q = 0$).

The three-phase equations of the grid-side circuit are listed in Eqs. (59–61):

$$v_{ga} = R_f.i_{ga} + L_f \frac{di_{ga}}{dt} + e_{fa} \tag{59}$$

$$v_{gb} = R_f.i_{gb} + L_f \frac{di_{gb}}{dt} + e_{fb} \tag{60}$$

$$v_{gc} = R_f.i_{gc} + L_f \frac{di_{gc}}{dt} + e_{fc} \tag{61}$$

Transforming the equations to the synchronous rotating frame, the d-q representation can be derived as:

$$v_{fd} = -R_f.i_{fd} - L_f \frac{di_{fd}}{dt} + e_{fd} \tag{62}$$

$$v_{fq} = -R_f.i_{fq} - L_f \frac{di_{fq}}{dt} - e_{fq} \tag{63}$$

where

$$e_{fd} = \omega_s.L_f.i_{fq} \tag{64}$$

$$e_{fq} = -\omega_s.L_f.i_{fd} + v_{gq} \tag{65}$$

The GSC allows the control of the RL filter currents i_{fd} and i_{fq} independently, and the latter is done by PSO-PI controller based on the reference value $i_{fd}*$ and $i_{fq}*$. Knowing that the active and reactive powers from the GSC are given by:

$$P_f = V_{fd}.I_{fd} + V_{fq}.I_{fq} \tag{66}$$

$$Q_f = V_{fq}.I_{fd} + V_{fd}.I_{fq} \tag{67}$$

By neglecting the losses due to the RL filter resistance while considering that the voltage vector is aligned with the q-axis of the synchronous rotating frame, the d-q voltage components are obtained as:

$$v_{sd} = 0, v_{sq} = \widehat{v_g}.$$

The active and reactive powers and the reference active and reactive powers are given as:

$$P_f = V_{sq}.I_{fq} \tag{68}$$

$$Q_f = V_{sq}.I_{fd} \tag{69}$$

$$P_f^* = I_{fq}^*.V_{sq} \tag{70}$$

$$Q_f^* = I_{fd}^*.V_{sq} \tag{71}$$

The power in the DC bus is divided into:

$$P_{RSC} = V_{dc}.I_{RSC} \tag{72}$$

$$P_C = V_{dc}.I_c \tag{73}$$

$$P_{GSC} = V_{dc}.I_{GSC} \tag{74}$$

$$P_{RSC} = P_c + Joule \tag{75}$$

By neglecting power losses due to the joule effect in the capacitor, the converters and the RL fil become and P_f becomes equal, and hence controlling P_f means controlling P_c which also translates into controlling the DC bus voltage (V_{dc}). As seen in the GSC Simulink model (Fig. 18), the dc-link voltage is controlled by the rotor q current component. Table 4 (see Appendix) lists the different parameters of the wind system.

PSO-PI control

PI controllers are widely used in the industry thanks to their simple design and good performance. The controller uses the error signal to generate a control command which is governed by the following equation:

$$u(t) = k_p e(t) + k_i \int e(t)d\tau \tag{76}$$

Fig. 17 Connection between the back-to-back converter and the grid

Fig. 18 Simulink model of the GSC control

Table 4 Parameters of the wind system

System	Parameter
Turbine	Number of blades:3 R = 45 m J_t = 1.4 .10^6 kg.m^2 V_n = 13 m/s, N_{tn} = 19 rpm
Gearbox	G = 100
DFIG	$U_r = U_s$ = 690 V P_n = 3 MW, f = 50 Hz, p = 2, Nr/Ns ≈ 1 R_s = 2.97 mΩ, R_r = 3.82 mΩ L_{fs} = 121 μH, L_{fr} = 57.3 μH, L_m = 12.12 mH J_g = 114 kg.m^2
DC bus	C = 38 mF, V_{dc} = 1200 V
RL filter	R_f = 0.75 Ω, L_f = 0.75 mH
Grid	U = 690 V, f = 50 Hz
MPPT	λ_{opt} = 7.07 C_{pmax} = 0.35
Rotor currents	Response time: t_r = 0.05 s K_{pr} = 3.σ.$\frac{L_r}{t_r}$ ≈ 0.01062 K_{ir} = 3.$\frac{R_r}{t_r}$ ≈ 0.2292
Stator currents	Response time: t_{rf} = 0.01 s K_{pf} = 3.$\frac{L_f}{t_{rf}}$ ≈ 0.3 K_{if} = 3.$\frac{R_{rf}}{t_{rf}}$ ≈ 30

where k_p and k_i are the proportional and integral gains and e(t) is the error. The discrete form of the PI has been used in this work where the control law is obtained using the trapezoid discretization method with T_s as sampling time. It is often hard to properly tune the gains of the controller; therefore, the proportional and integral actions are optimized by an improved PSO. This meta-heuristic approach is a well-established technique. The algorithm relies on the principle of swarm social behavior, where the swarm contains several

particles that represent potential solutions. Each particle is characterized by a position p_i and a velocity v_i, and the objective is to find the velocity that moves particles toward the optimal position. Further details can be found in (Kebbati et al. 2021a, b), and the algorithm is governed by the velocity and position update equations:

$$\begin{cases} v_i(k+1) = \omega v_i(k) + c_1 r_1 \left(Pb_i(k) - x_i(k) \right) + c_2 r_2 \left(Gb_i(k) - x_i(k) \right) \\ x_{i(k+1)} = x_{i(k)} + v_i(K+1) \end{cases} \quad (77)$$

where ω is known as inertia weight, and c_1 and c_2 are known as cognitive and social accelerations coefficients, respectively. $r_{1,2} \in [0, 1]$ are random constants, and Gb and Pb represent the global best position of the whole swarm and the local best position in the current swarm generation. In the classic PSO, the inertia weight, social and cognitive accelerations are prefixed constants. However, in the improved version of this work they are dynamic and change with iterations according to Eqs. (3.76, 3.77), and this enhances the PSO search performance:

$$\omega = \omega_{min} + \frac{\exp\left(\omega_{max} - \lambda_1 \left(\omega_{max} + \omega_{min} \right) \frac{g}{G} \right)}{\lambda_2} \quad (78)$$

$$\begin{cases} c_1(k+1) = c_1(k) + \alpha \\ c2(k+1) = c_2(k) + \beta \\ \alpha = -2\beta = 0.085 \, for \, \frac{g}{G} \leq 30\% \\ \alpha = \frac{-\beta}{2} = 0.045 \, for \, 30\% \leq \frac{g}{G} \leq 60\% \\ \alpha = -\frac{\beta}{2} = -0.025 \, for \, 60\% \leq \frac{g}{G} \leq 85\% \\ \alpha = -\beta = -0.0025 \, for \, \frac{g}{G} \geq 85\% \end{cases} \quad (79)$$

The terms g and G represent the actual and the last generations, respectively, and $\lambda_{1,2}$ are constant parameters adjusted to ensure an exponential decrease from ω_{max} to ω_{min} which are maximum and minimum inertia weights. The advantage of this improved version compared to other versions is

that it increases the overall search capabilities of the PSO algorithm, as the exponential decrease of ω accelerates the convergence toward the global best solution. Increasing c_1 pulls the particles toward Pb and enhances the exploration phase, while increasing c_2 speeds the convergence toward Gb which enhances the exploitation phase and vice versa. The proposed PSO is used to optimize the PI actions $\{k_p, k_i\}$ applied to the complete model. The approach is illustrated in Fig. 19 where the mean squared error (MSE) is used as the fitness function for the PSO algorithm. The model is simulated with the gains obtained from the PSO algorithm, which are optimized at every iteration until the optimal solution is found. (Kebbati et al. 2021a, b) applied the PSO algorithm to optimize a model predictive controller for path tracking applications in autonomous vehicles. The same algorithm was implemented in (Kebbati et al. 2022) to tune a PID controller for autonomous driving applications.

The optimization with improved PSO resulted in the gains $\{k_{p1} = 5.6749, k_{i1} = 11.6077\}$ for the inverter controller and the gains $\{k_{p2} = 3.4074, k_{i2} = 9.4171\}$ for the DFIG controller, while the optimized gains for the grid-side converter were found as $\{k_{p3} = 7.6999, k_{i3} = 5.019\}$.

Economic and environmental analysis

In this study, the hybrid system is of large scale and injects power directly into the grid. Such systems have very high initial investments but pay off in the long run. The size of the system is important in determining the feasibility and cost-eff of the whole project. In general, the cost of any system is composed of capital costs, replacement, operating and maintenance costs. The capital cost must include the price

for all the components of the system as well as transportation, packaging and installation of these components, etc. The capital cost is given by the following formula:

$$\text{Capital cost} = (1 + K).N.C \tag{80}$$

where C and K are the cost of one component (PV panel, wind turbine, etc.) and the cost related to engineering, logistics, installation, etc. N represents the number of components (100 PV panels, 30 converters, etc.). On the other hand, the replacement and operating and maintenance costs are known as variable costs. The operating and maintenance costs include the expenses of insurance, salary of operators, taxes, recurring costs and maintenance. They are expressed as a percentage of the initial capital cost. The replacement costs are the expenses needed to change components as these have different lifetimes and some of them requires to be replaced several times during the lifespan of the system. When conducting economic analyses of energy systems, the main factor for judging if the system is feasible or not is the levelized cost of electricity (LCOE). The latter represents the cost of generated energy units during the lifespan of the system. The LCOE is calculated by summing the capital costs and operating and maintenance costs and dividing by the total energy generated from the system. The net present value (NPV) approach is used for the calculation of the LCOE. In this method, the total expenses and the incomes of the system are determined based on discounting from a starting date, and the LCOE is given as:

Fig. 19 PSO-PI control approach
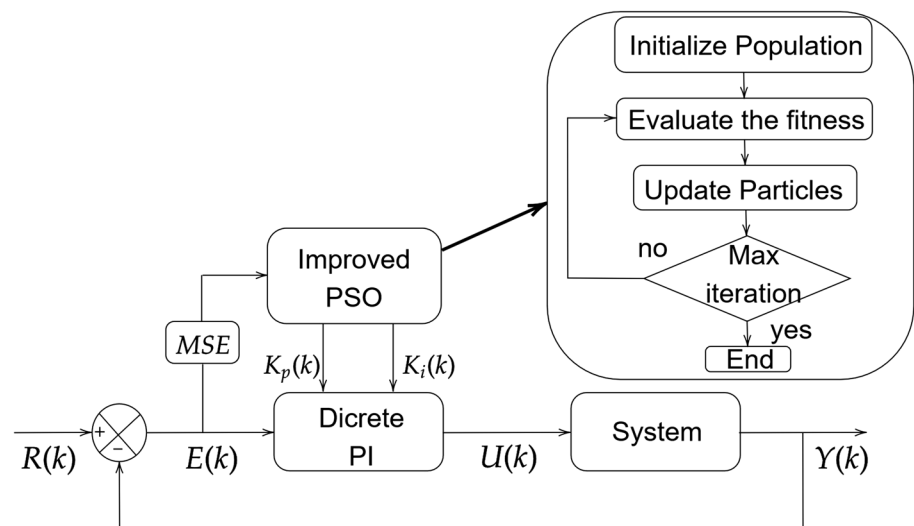
$$\text{LCOE} = \frac{I_0 + \sum_{t=1}^{n} \frac{A_t}{(1+i)^t}}{\sum_{t=1}^{n} \frac{M_{t,el}}{(1+i)^t}} \qquad (81)$$

where I_0, A_t and $M_{t,el}$ are the respective investment expenditure, annual total cost and produced quantity of electricity. i, n and t represent the interest rate, the economic operational lifetime and the year, respectively. The NPV measures the net profit and actual value of the project, and it includes all benefits and cost streams occurring at different points in time and converts them into present value equivalents. The NPV is calculated over a period of time by subtracting cash outflows from the values of cash inflows. The overall worth of the project is determined by the present value equivalents, and the formula for NPV is given as:

$$NPV = \sum_{t=1}^{n} \frac{R_t - C_t}{(1 + i)^t} - I_0 \qquad (82)$$

where R_t and C_t represent the revenue and the costs in year t; i and I_0 are the discount rate and the initial investments,

respectively. The payback time represents the time required for the system to amortize the initial project investment by its cash inflows. Shorter payback times ensure a faster recovery of the investment funds. Generally, the distribution of cash flow is not considered beyond the payback period. The payback time can be calculated using the following equation:

$$\text{Payback period} = \frac{\text{Initial Investment}}{\text{Cash inflow per period}} \qquad (83)$$

System model in HOMER

Homer is used to perform an economic and environmental analysis of the system, which is supposed to inject all its power into the grid. Thus, all produced electricity will be sold to the utility. The different system components are shown in Fig. 20 and listed with their respective costs in Table 5. The cost of engineering, logistics and installation has been estimated at 25% of the component's cost. The interest rate is set to 3.75%, while the inflation rate is
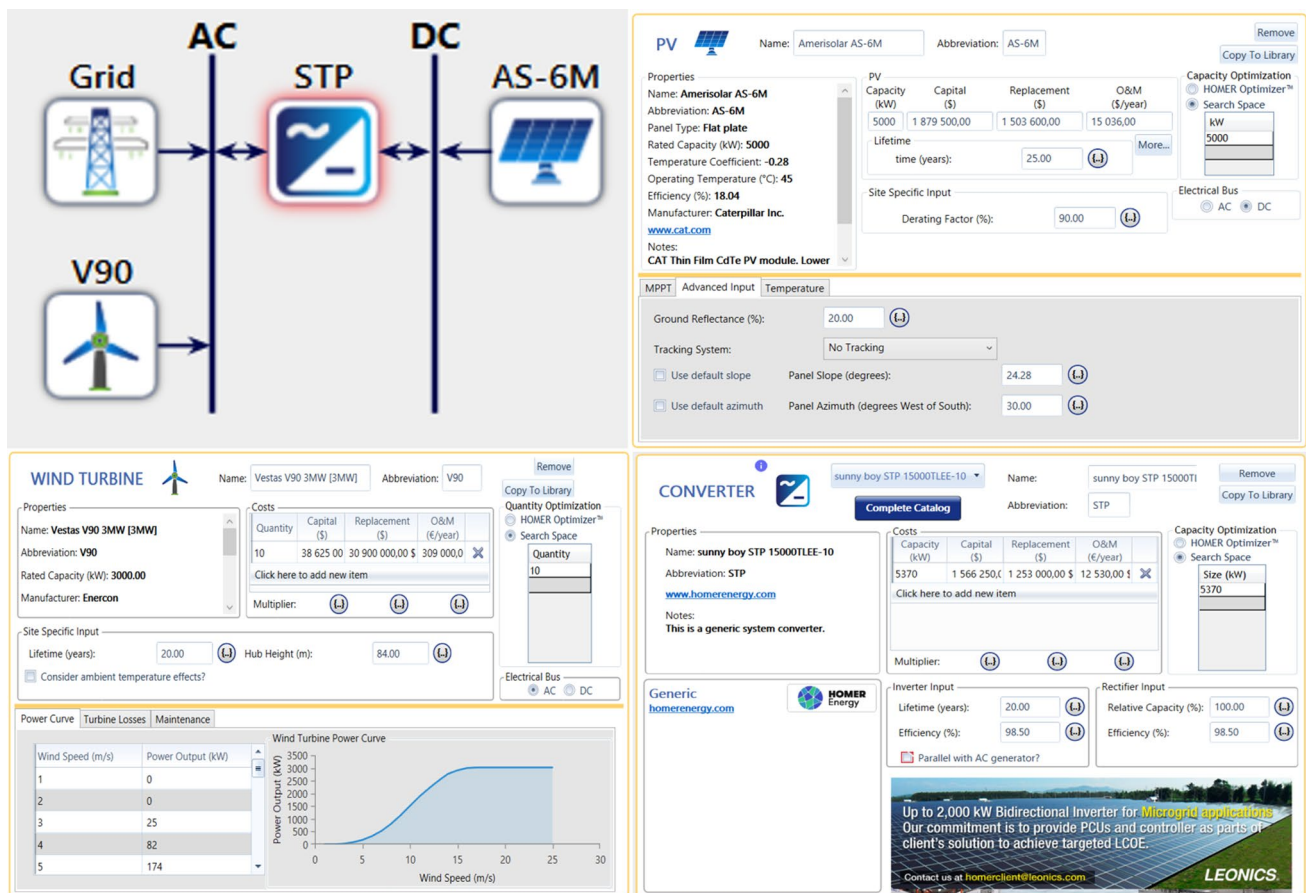
Fig. 20 Homer model of the hybrid system

evaluated at 2.42% (Ministry of finance 2021). Moreover, the electricity price is fixed at 0.04 \$/kWh. Electricity producers using solar and wind energies benefit from a premium of 300% of the market price of electricity; this is ensured for the full project lifetime according to law "No.° 02–01 du 22 Dhou El Kaada 1422 (Articles 88 ff)" (Meyer-Renschhausen 2013).

For the environmental analysis, the amount of sulfur dioxide and nitrogen oxides emitted by a combined cycle power plant using natural gas has been chosen as 2.74 kg/MWh and 1.34 kg/MWh, while the amount of CO_2 is estimated at 400 kg/MWh (Benhadji Serradj et al. 2021 et al. 2021).

Results and discussion

The system is simulated for two specific months using hourly data that was generated by METEONORM. The result is hourly power output; the latter is compared to hourly power production of the central power plant of Adrar. The inputs to the PV system are global horizontal irradiation, direct normal irradiation, diffuse horizontal irradiation and the number of hours. The outputs are active and reactive powers. On the other hand, the wind system receives hourly wind speeds, and outputs active and reactive powers as well. The performance of the control is presented along with the energy output of the PV plant and the wind farm. An analysis of the amount of power injected into the grid and the contribution

Table 5 Summary of the system costs

Component	Capital cost ($)	Replacement cost ($)	OMC (%)
PV panel (AS-6 M)	132	105	1
Wind turbine (Vestas V90)	3,862,500	3,090,000	1
DC/AC converter (Sunny boy STP 15,000)	4375	3500	1

Fig. 21 PV cell temperature variations (January vs August)
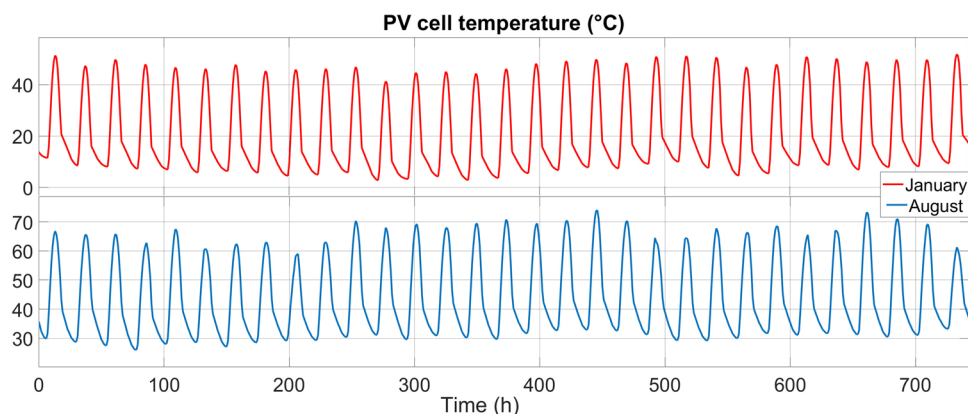
Fig. 22 Irradiance received by the PV modules (January vs August)
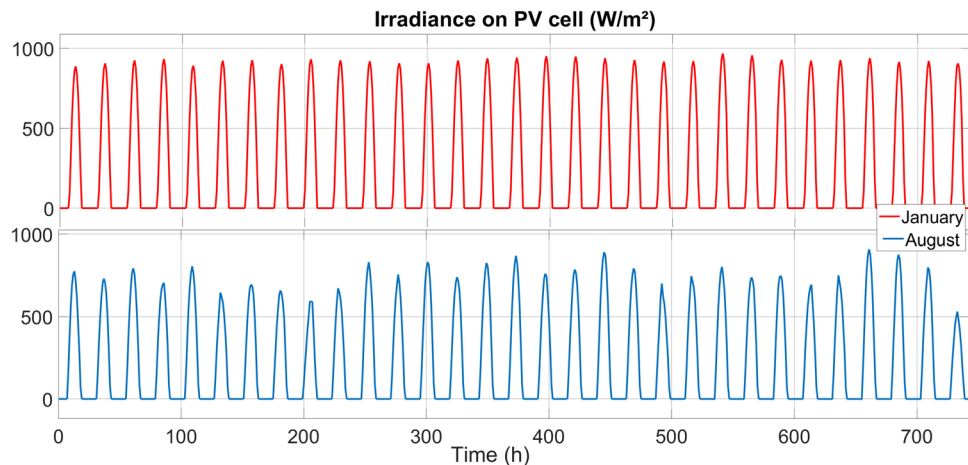
of the hybrid system is also conducted. The performance output of the PV system is affected mainly by the cell's temperature and the irradiation received by the PV generator, the temperature lowers the efficiency. The trend of cell temperature levels in January shows slight variations. Peak levels vary each day with a maximum of 52 °C at the beginning and the end of the month, and a minimum of 41 °C is noticed around mid-January. Figure 21 shows hourly variations of cell temperature in January versus August.

Although ambient temperatures in January are significantly low, the irradiation received by the module is unpredictably high (see Fig. 22). Minimum radiation levels of around 850 W/m^2 are observed in the first and last days of January; this can be attributed to the solar position throughout the year as the distance between the earth and the sun varies and leads to a variation of extraterrestrial radiation flux. Irradiation levels in August are considerably low compared to January; low irradiation coupled with high temperatures reduces dramatically the PV output.

MPPT control performance for PV system

The perturb and observe algorithm keeps the voltage output of the PV module at its maximum value, the accuracy is determined by the size of the perturbation (ΔV), and thus, the output keeps oscillating around the maximum value as demonstrated in Fig. 23. It is worth mentioning that the MPPT tracker is fast, and the maximum power point is quickly reached; hence, the control works perfectly.

Figure 24 shows how the power output of the PV module follows the maximum power point under standard test conditions (STC) ($G = 1000$ W/m^2 and $T_c = 25$ °C).

DC-DC converter control

The boost converter control maintains V_{dc} constant all the time as observed in Fig. 25, and the latter will be received by the inverter to be converted into AC form.

Active and reactive power control for PV system

The performance of the PV system power control is shown in Fig. 26; both active (P) and reactive (Q) powers follow exactly the reference values. Negative values imply that the energy is injected into the grid, while positive values mean that the energy is drawn from the grid. The reactive power is kept around zero to ensure unity power factor. The amount
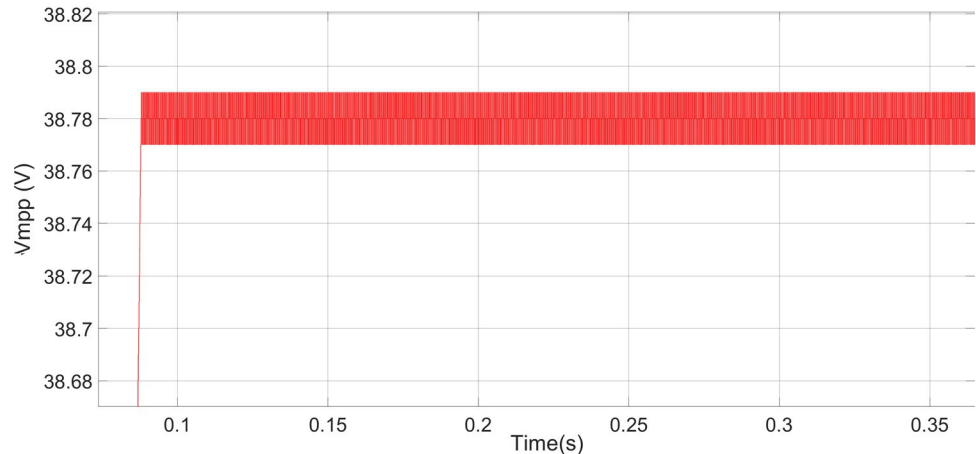
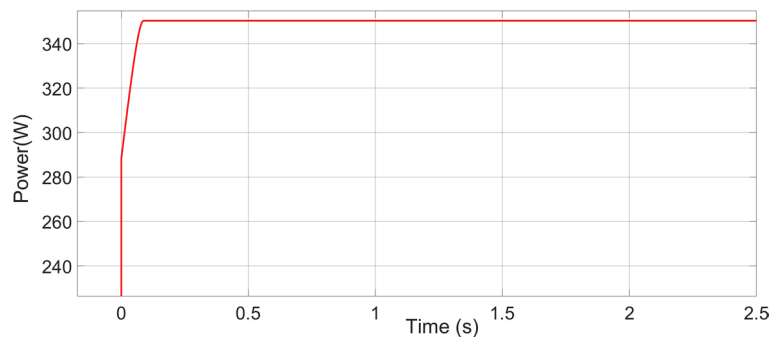**Fig. 23** Performance of the MPPT tracker

Fig. 24 PV panel power output at STC
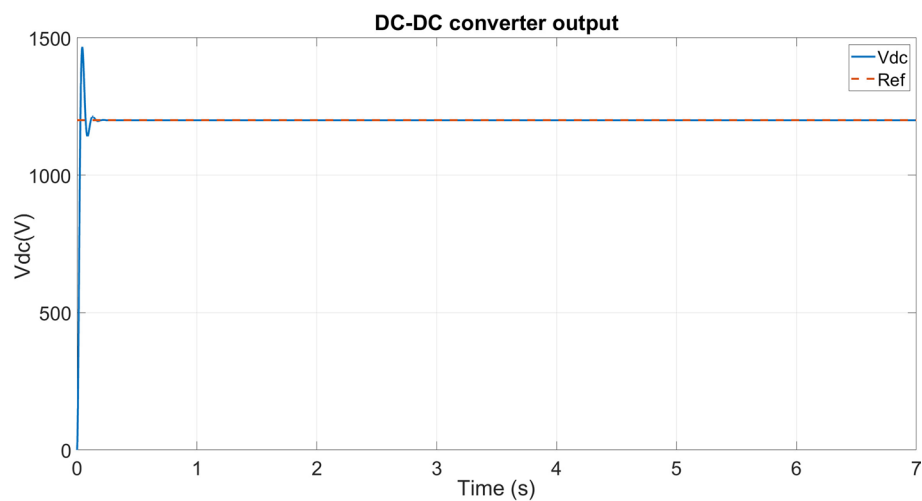
Fig. 25 DC-DC converter output

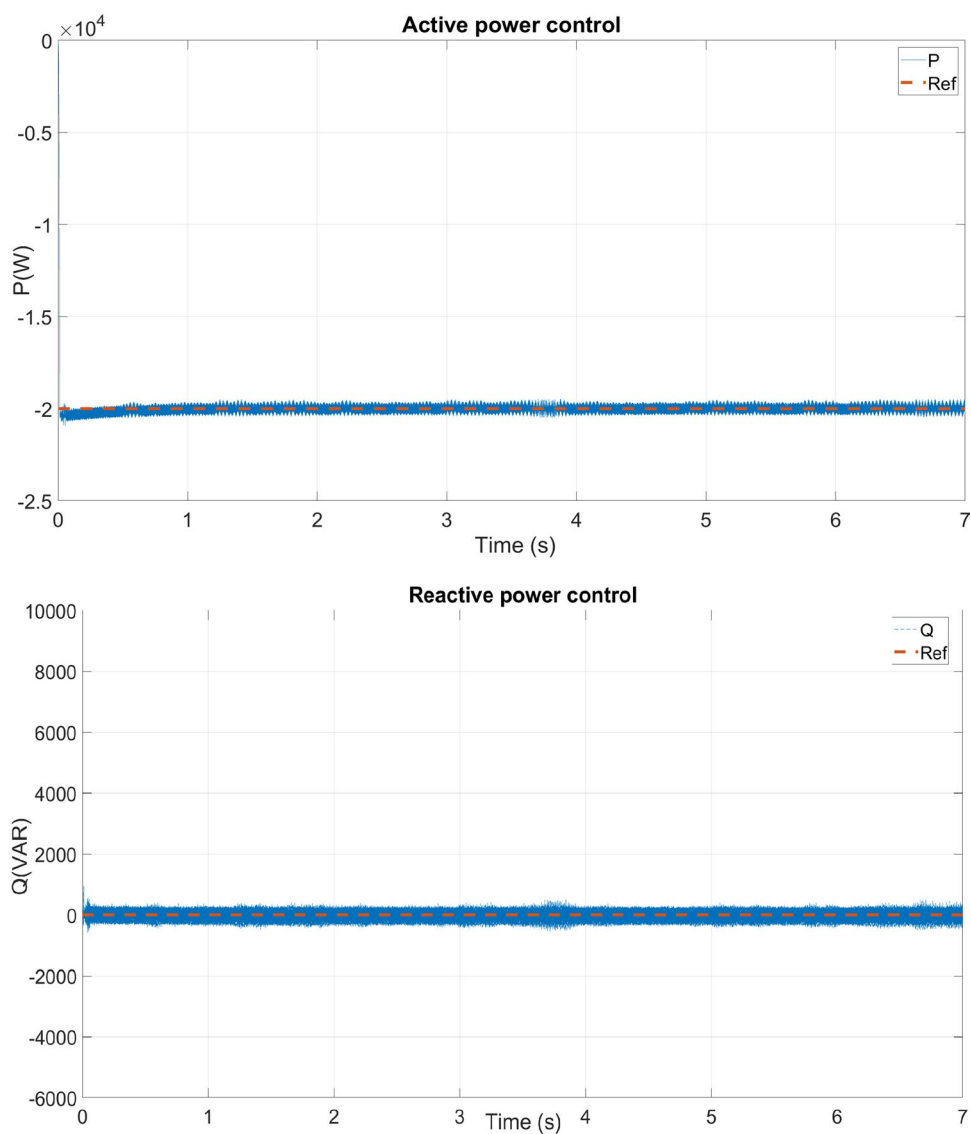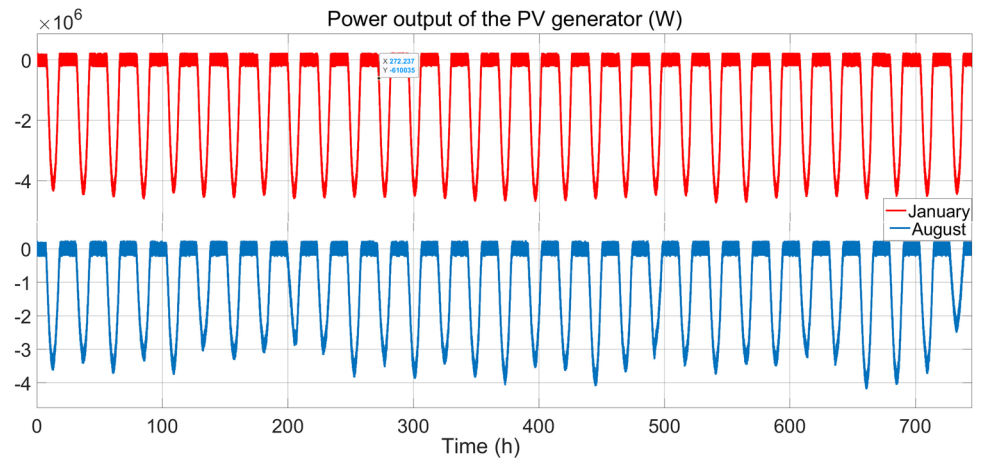**Fig. 26** Power control for the PV system

Fig. 27 Power output of the PV plant (January vs August)

of power generated corresponds to one string under STC conditions, which is equivalent to 14 KW.

Output of the PV plant

The simulation results for January show that the PV generator produced from 4.35 MW to 4.73 MW depending on the day, irradiation and temperature levels (see Fig. 27). The power is produced from 7 am to 6 pm with peak production occurring between midday and 2 pm. During the month of August, the PV generator produces less power compared to January. This decrease in power output is justified by the high temperatures which reduce the efficiency of the PV generators. Peak production ranges from 2.45 MW to 4.15 MW. However, the production during the day lasts from 7 am to 7 pm delivering power for an extra hour compared to January, since summer days are longer than winter days.

The wind system has a rated power of 30 MW, which depends on the speed of the wind. The turbine's pitch angle is fixed at its optimal value and the hub height is fixed at 80 m, where the corresponding wind speeds are shown

in Fig. 28. In August, the wind speed profile shows more energy potential as high speeds occur more frequently. The average speed is around 8 m/s, meaning that the system should generate more energy in August than in January. Thus, the performance of the grid should be improved in this period of time that corresponds with high demand.

MPPT control performance for wind system

The MPPT implemented to control the rotation speed of the turbine was tested with a multitude of different reference values and the result is presented in Fig. 29. The PSO-PI performs very well ensuring maximum power extraction from the wind. As observed, the rotational speed follows exactly the reference values, and the robustness of the control is tested by changing the reference values every time. Figure 30 shows the performance of the wind system power control. In the first graph of Fig. 30, the active power follows exactly the given reference values. The reference values in the system are obtained from the mechanical model as explained in the control section.
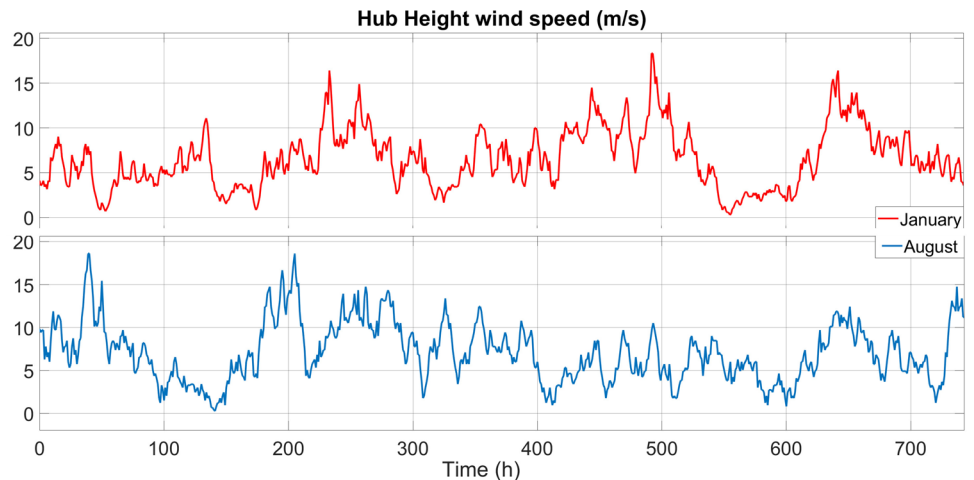
Fig. 28 Wind speeds at hub height (January vs August)

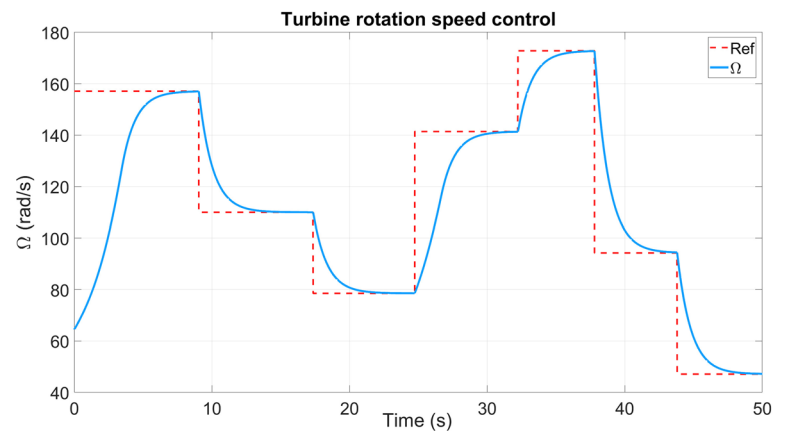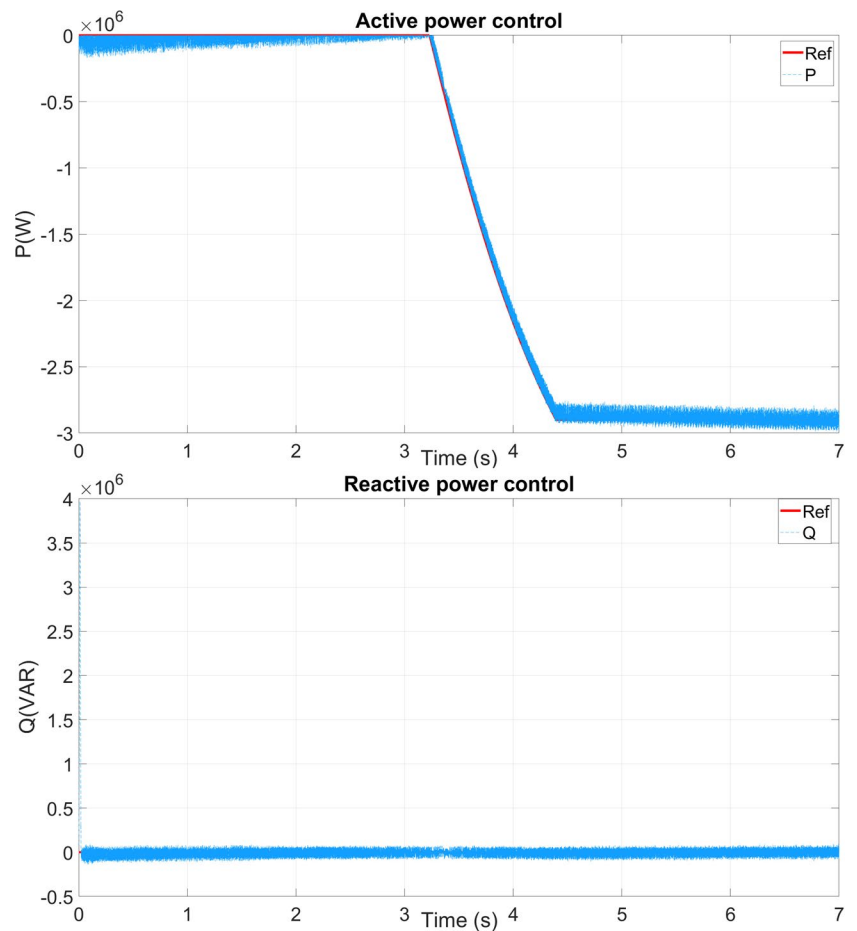**Fig. 29** MPPT turbine rotation speed tracking

Fig. 30 Power control for the wind system

In the second graph of Fig. 30, the reactive power is maintained at zero which ensure a unity power factor.

Output of the wind farm

January is characterized by lower wind speeds; hence, the power output is lower compared to August, as seen in Fig. 31. Peak production is reached in three weeks out of four with an output ranging from 10 to 23 MW. During August, more power was produced and the rated output was often reached especially in the beginning and at the end of the month. An average of around 10 to 25 MW is maintained throughout the month. This amount of power will contribute significantly to grid performance as the cooling load increases during this month.

Fig. 31 Power output of the wind farm (January vs August)
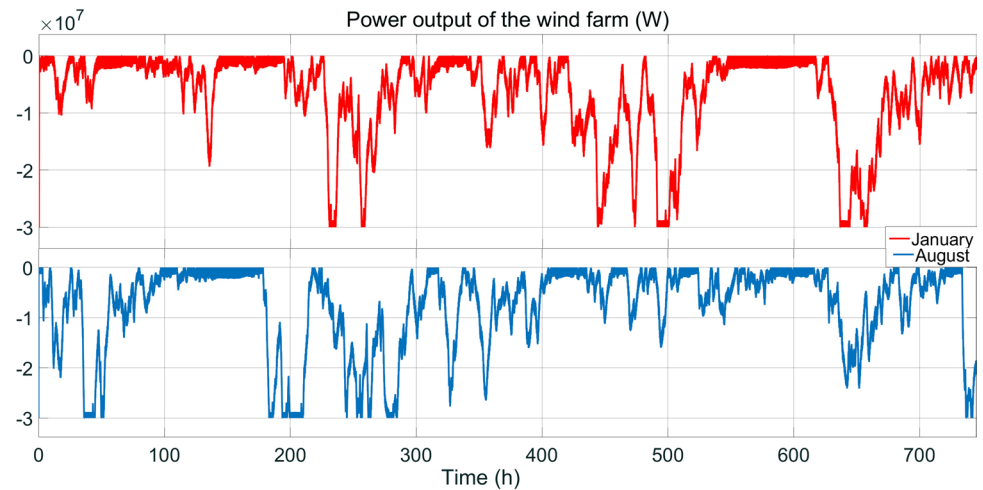
Fig. 32 System power output vs central plant power production (January vs August)
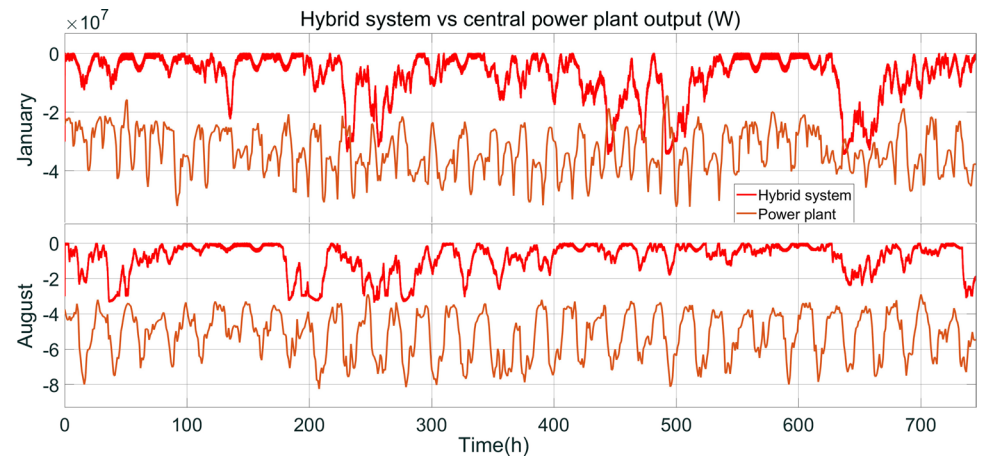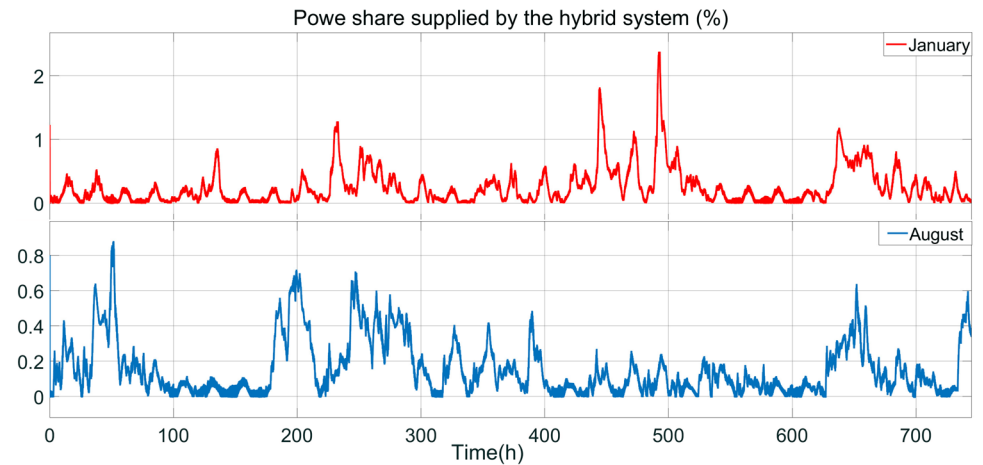

**Fig. 33** Share covered by the hybrid system (January vs August)

Results of the hybrid system

The power produced by the hybrid system is compared to that produced by the central power plant of Adrar to

determine the contribution of the system to the grid (see Fig. 32). More contribution is achieved in January varying from 10 to 34.5 MW, while less contribution was achieved in August due to higher energy demand. The peak loads

Fig. 34 Cumulative cash flow of the project
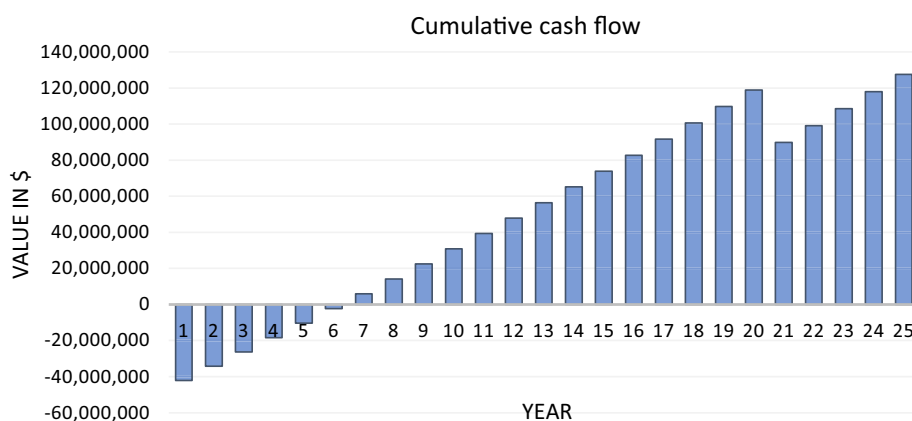
Table 6 Reduced GHG emissions

Gas	Emissions reduction (kg/year)
Carbon dioxide (CO_2)	28 393 342
Sulfur dioxide (SO_2)	194 494
Nitrogen oxides (NO_x)	95 118

seemed to appear from 2 to 9 pm, while the lowest production occurs between 2 am and 10 pm. Despite the high power produced by the hybrid system, it is still low visa-vis the central power plant. However, on most days the hybrid system managed to cover up to 50% of what the plant produces.

Figure 33 shows the amount of power covered by the hybrid system. In January, the hybrid system covered from 50 to 220% of what the central power plant produced, while in August, the share covered by the system varies from 20 to 85%. Note that the central power plant supplies power to the whole province of Adrar; in reality, the true load of Adrar city is much lower.

Cost analysis

HOMER results show from an economical point of view that the system composed of a 5-MW rated PV system and a 30-MW rated wind system has a total net present value (NPV) of $167 million, whereas the levelized cost of electricity (LCOE) sits at 0.084 $/kWh. The LCOE is very profitable compared to the selling price of 0.114 $/kWh guaranteed by the feed-in tariff for the duration of the project. As a result, the payback period is in just 7.3 years and by the end of the projects lifetime a cumulative net profit of $127 million is reached. Figure 34 depicts the cash flow over the lifespan of the project, which shows how much money is either spent on or gained by the project.

The initial investment for implementing the project is evaluated at $42.1 million, and the total operating and maintenance cost of the whole system for 25 years is $7.46 million. It was found that the PV system and the set of converters each cost initially 4% of the initial investment, while the rest of the cost is attributed to the wind turbines.

The wind system dominates the share of both capital cost and operating and maintenance costs as seen in Fig. 35. Both PV system and converts account for 4% each of the total
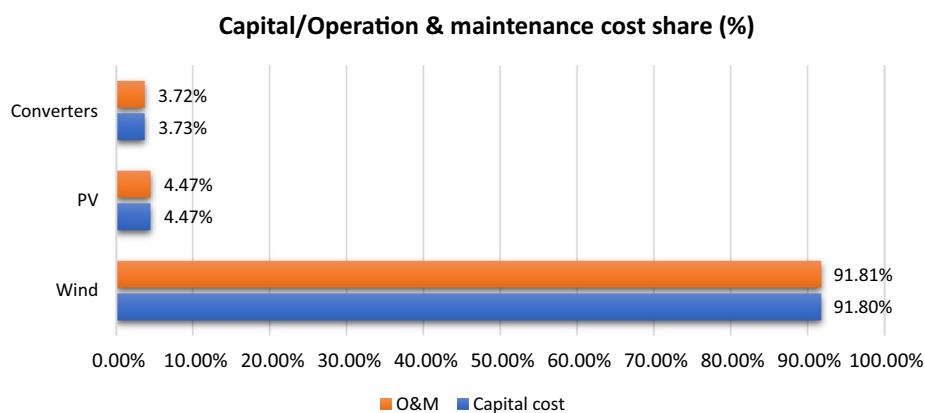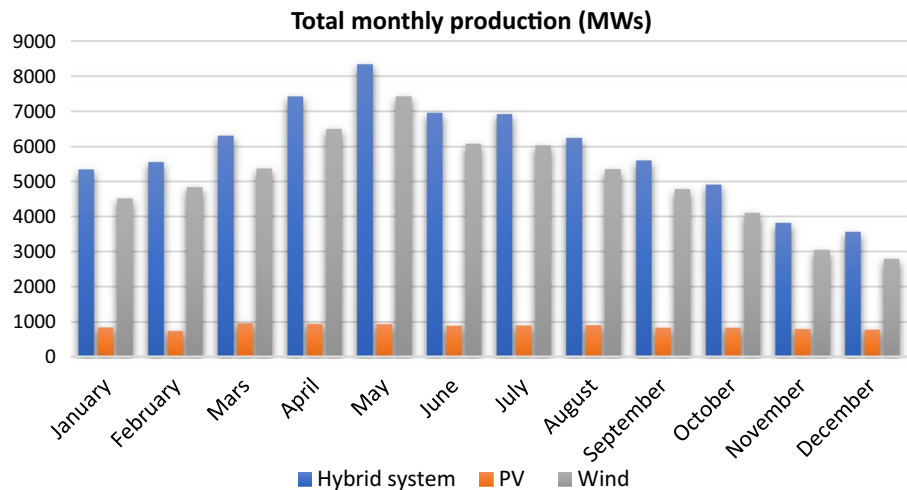
Fig. 35 Components share of the total cost

Fig. 36 Monthly power production

capital cost compared to 92% for the wind system. For every year of the project lifetime, the operating and maintenance of the PV array and converters require yearly around $15,036 and $12,530, respectively. On the other hand, the wind turbines require $309,000 representing 91.8% of the total cost. Furthermore, the PV system produces 14.5% of to the total power generation versus 85.5% coming from the wind system. The monthly power production of both systems is shown in Fig. 36. There is a big difference in energy contribution that depends on two main factors: the different size of each system and the difference in the respective energy potential over the year.

Environmental impact

From the environmental aspect, the designed system has a significant positive impact on the environment over the conventional power plant. It was found that implementing the hybrid system yields a remarkable reduction in harmful GHG emissions including CO_2, SO_2 and NO_x. For instance, a general gas-based combined cycle power plant produces around 400 kg/MWh. Therefore, integrating the system to the grid would dramatically reduce the amount of emitted GHG given the fact that electricity production in Algeria is mainly based on natural gas. Such emission reductions contribute to mitigating global warming and climate change. Table 6 summarizes the amounts of avoided emissions.

Conclusion

This article has addressed the design, modeling and control of a large-scale hybrid PV-wind grid-connected system. The developed system has been tested for the Adrar region

situated in the Algerian desert due to its relevant wind and solar energy resources. An innovative control approach using optimized PSO-PI controllers has been proposed to control the different inverters and converters of the wind turbines and PV system, where a new improved PSO algorithm is implemented to enhance the performance of the controllers. The performance of the designed system was assessed using hourly weather data for January and August. These two months represent the critical periods of winter and summer where the energy demand and energy resources vary the most. To evaluate the contribution of the system to the grid, its generated power was compared to the one generated by the central power plant of the region in question. It was found that the system is able to cover an important share of the total power consumption in the region, but it mostly depends on energy resource variations. Furthermore, an economic feasibility and environmental impact of the hybrid system was carried out using HOMER. The results showed that the developed system proved to be technically and economically feasible. From an economical point of view, the project is cost-effective, with short a pay-back time and significant long-term profits. The environmental analysis revealed that implementing this project yields a significant yearly reduction in GHG emissions. The proposed hybrid system is an adequate solution to power shortages and grid problems faced in the region of Adrar during hot seasons. The proposed solution falls in line with the plan of Algeria to integrate wind and solar energy in its energy mix by 2030.

Appendix

See Tables 2, 3, 4

Declarations

Conflict of interest The authors emphasize that there are no conflicts of interest about the publication of this article.

References

Abada Z, Bouharkat M (2018) Study of management strategy of energy resources in Algeria. Energy Rep 4:1–7. https://doi.org/10.1016/j.egyr.2017.09.004

Benhadji Serradj DE, Sebitosi AB, Fadlallah SO (2021) Design and performance analysis of a parabolic trough power plant under the climatological conditions of Tamanrasset, Algeria. Int J Environ Sci Technol. https://doi.org/10.1007/s13762-021-03350-x

Boudia SM, Benmansour A, Hellal MAT (2016) Wind resource assessment in Algeria. Sustain Cities Soc 22:171–183. https://doi.org/10.1016/j.scs.2016.02.010

Bouraiou A, Necaibia A, Boutasseta N, Mekhilef S, Dabou R, Ziane A, Touaba O (2020) Status of renewable energy potential and utilization in Algeria. J Clean Prod 246:119011. https://doi.org/10.1016/j.jclepro.2019.119011

Bouzidi B (2011) Viability of solar or wind for water pumping systems in the Algerian Sahara regions–case study Adrar. Renew Sustain Energy Rev 15(9):4436–4442. https://doi.org/10.1016/j.rser.2011.07.108

Charrouf O, Betka A, Becherif M, Tabanjat A (2018) Techno-economic analysis of wind turbines in Algeria. Int J Emerg Electric Power Syst. https://doi.org/10.1515/ijeeps-2017-0178

Corry J, Ferroukhi R, Garcia Banos C, Jordan M, Khalid A, Reeves A, Renner M, Taylor M (2016) "Renewables 2016 global status report," *REN21 2016*

Dabou R, Bouchafaa F, Arab AH, Bouraiou A, Draou MD, Neçaibia A, Mostefaoui M (2016) Monitoring and performance analysis of grid connected photovoltaic under different climatic conditions in south Algeria. Energy Convers Manage 130:200–206. https://doi.org/10.1016/j.enconman.2016.10.058

Dekali Z, Baghli L, Boumediene A (2021) Experimental implementation of the maximum power point tracking algorithm for a connected wind turbine emulator. Revue Roumaine Des Sciences Techniques. Serie Électrotechnique Et Énergétique 66(2):111–117

Dhimish M, Alrashidi A (2020) Photovoltaic degradation rate affected by different weather conditions: a case study based on PV systems in the UK and Australia. Electronics 9(4):650

Djamai M, Merzouk NK (2011) Wind farm feasibility study and site selection in Adrar, Algeria. Energy Procedia 6:136–142. https://doi.org/10.1016/j.egypro.2011.05.016

Fadlallah SO, Serradj DEB, Sedzro DM (2021) Is this the right time for Sudan to replace diesel-powered generator systems with wind turbines? Renew Energy 180:40–54

Gaillard A (2010) *Système éolien basé sur une MADA: contribution à l'étude de la qualité de l'énergie électrique et de la continuité de service* (Doctoral dissertation, Université Henri Poincaré-Nancy 1)

Genç MS (2011) Economic viability of water pumping systems supplied by wind energy conversion and diesel generator systems in North Central Anatolia, Turkey. J Energy Eng 137(1):21–35

Genç MS, Karipoğlu F, Koca K, Azgın ŞT (2021) Suitable site selection for offshore wind farms in Turkey's seas: GIS-MCDM based approach. Earth Sci Inf 14(3):1213–1225

Genç MS (2021) Determination of the most appropriate site selection of wind power plants-based Geographic Information System and Multi-Criteria Decision-Making approach in Develi, Turkey. International Journal of Sustainable Energy Planning and Management, 30

GlobalPetrolPrices.com (2020) Sudan Diesel prices. Global Petrol Prices. Retrieved from https://www.globalpetrolprices.com/Sudan/diesel_prices/. Accessed Feb 2021

GlobalPetrolPrices.com (2020), "Electricity prices around the world," 2018. [Online]. Available: https://www.globalenergyprices.com/en/electricity-prices/. Accessed 28 July 2021

Gökçek M, Genç MS (2009) Evaluation of electricity generation and energy cost of wind energy conversion systems (WECSs) in Central Turkey. Appl Energy 86(12):2731–2739

Harrouz A, Abbes M, Colak I, Kayisli K (2017) Smart grid and renewable energy in Algeria. In *2017 IEEE 6th International Conference on Renewable Energy Research and Applications (ICRERA)* (pp. 1166–1171). IEEE. https://doi.org/10.1109/ICRERA.2017.8191237

Himri Y, Merzouk M, Merzouk NK, Himri S (2020) Potential and economic feasibility of wind energy in south West region of Algeria. Sustain Energy Technol Assess 38:100643. https://doi.org/10.1016/j.seta.2020.100643

Isen E, Bakan AF (2016) Development of 10 kW Three-Phase Grid Connected Inverter. Automatika 57(2):319–328. https://doi.org/10.7305/automatika.2016.10.1081

Kabir E, Kumar P, Kumar S, Adelodun AA, Kim KH (2018) Solar energy: potential and future prospects. Renew Sustain Energy Rev 82:894–900. https://doi.org/10.1016/j.rser.2017.09.094

Kebbati Y, Puig V, Ait-oufroukh N, Vigneron V, Ichalal D (2021a) "Optimized adaptive MPC for lateral control of autonomous vehicles," 2021a 9th Int. Conf. Control. Mechatronics Autom. ICCMA 2021a

Kebbati Y, Ait-oufroukh N, Vigneron V, Ichalal, D (2021b) "Neural Network and ANFIS based auto-adaptive MPC for path tracking in autonomous vehicles," 2021b 18th IEEE Int. Conf. Networking, Sens. Control. ICNSC 2021b

Kebbati Y, Ait-oufroukh N, Vigneron V, Ichalal D (2022) coordinated pso-pid based longitudinal control and MPC based lateral control for autonomous vehicles. In: 2022 20th European Control Conference (ECC). IEEE, pp 1–6

Kidar A, Kouzou A, Kaddouri AM, Hafaifa A, Saadi S (2021) The implementation Feasibility of PV Power Plant based on Mono-Crystalline and Poly-Crystalline Technologies for remote regions in the Algerian Steppe. Electrotehnica Electronica Automatica 69(3):30–38. https://doi.org/10.46904/eea.21.69.3.1108004

Kumar R, Ismail M, Zhao W et al (2021) Damage detection of wind turbine system based on signal processing approach: a critical review. Clean Techn Environ Policy 23:561–580. https://doi.org/10.1007/s10098-020-02003-w

Maouedj R, Mammeri A, Draou MD, Benyoucef B (2015) Techno-economic analysis of a standalone hybrid photovoltaic-wind system. Application in electrification of a house in Adrar region. Energy Procedia 74:1192–1204. https://doi.org/10.1016/j.egypro.2015.07.762

Meyer-Renschhausen MARTIN (2013) Evaluation of feed-in tariff-schemes in African countries. J Energy Southern Africa, 24(1)

Meyers J, Meneveau C (2012) Optimal turbine spacing in fully developed wind farm boundary layers. Wind Energ 15:305–317

Ministry of Finance, "Taux d'inflation," *Ministry of finance*, 2021. [Online]. Available: http://www.mf.gov.dz/index.php. [Accessed: 3-Dec-2021]

Mourad L (2016) *Synthèse de lois de commande non-linéaires pour le contrôle d'une machine asynchrone à double alimentation dédiée à un système aérogénérateur* (Doctoral dissertation, Ph. D. thesis, Université Aboubakr Belkaid–Tlemcen–Faculté de Technologie)

Index Mundi (2021) CIA World Factbook. http://www.indexmundi.com/g/r.aspx?v=81000. Accessed Feb 2021

Mustapha G, Mohamed H, Achraf B (2018) "OPEC : Algeria," *Annual Statistical Bulletin 2018*. [Online]. Available: https://www.opec.org/opec_web/en/about_us/146.htm. [Accessed: 30-Jul-2018]

Nedjari HD, Haddouche SK, Balehouane A, Guerri O (2018) Optimal windy sites in Algeria: potential and perspectives. Energy 147:1240–1255. https://doi.org/10.1016/j.energy.2017.12.046

Podder AK, Roy NK, Pota HR (2019) MPPT methods for solar PV systems: a critical review based on tracking nature. IET Renew Power Gener 13(10):1615–1632

Serradj DB, Anderson TN, Nates RJ (2021) The use of passive baffles to increase the yield of a single slope solar still. Sol Energy 226:297–308

Shaltout MM, El-Hadad AA, Fadly MA, Hassan AF, Mahrous AM (2000) Determination of suitable types of solar cells for optimal outdoor performance in desert climate. Renew Energy 19(1–2):71–74. https://doi.org/10.1016/S0960-1481(99)00018-X

Shata AA, Hanitsch R (2006) Evaluation of wind energy potential and electricity generation on the coast of Mediterranean Sea in Egypt. Renew Energy 31(8):1183–1202

Singh G, Sundaram K, Matuonto M (2021) A solution to reduce overheating and increase wind turbine systems availability. Wind Eng 45(3):491–504

SolarPanelTilt.com (2021),"Optimum Tilt of Solar Panels." [Online]. Available: www.solarpaneltilt.com. Accessed 06 Dec 2021

Terfa H, Baghli L, Bhandari R (2022) Impact of renewable energy micro-power plants on power grids over Africa. Energy 238:121702. https://doi.org/10.1016/j.energy.2021.121702

Ministère de Transport (2008) "Recueil de Données," *Atlas Climatologique National*. Office national de la météorologie

Villalva MG, Gazoli JR, Ruppert Filho E (2009) Comprehensive approach to modeling and simulation of photovoltaic arrays. IEEE Trans Power Electron 24(5):1198–1208. https://doi.org/10.1109/TPEL.2009.2013862

Wang L, Kerrouche KDE, Mezouar A, Van Den Bossche A, Draou A, Boumediene L (2018) Feasibility study of wind farm grid-connected project in Algeria under grid fault conditions using d-facts devices. Appl Sci 8(11):2250. https://doi.org/10.3390/app8112250

Wijeratne WPU, Yang RJ, Too E, Wakefield R (2019) Design and development of distributed solar PV systems: Do the current tools work? Sustain Cities Soc 45:553–578

Yaneva M (2018) "Algeria's Adrar commissions 48 MW of solar power," *Renewables Now*, 2016. [Online]. Available: https://renewablesnow.com/news/algerias-adrar-commissions-48-mwof-solar-power-516499/. [Accessed: 12-Apr-2018].

Yoshino N, Taghizadeh-Hesary F, Otsuka M (2021) Covid-19 and optimal portfolio selection for investment in sustainable development goals. Financ Res Lett 38:101695. https://doi.org/10.1016/j.frl.2020.101695 (**ISSN 1544-6123**)

Zerglaine A, Mohammedi A, Mebarki NE, Rekioua D, Rekioua T (2021) Experimental investigation on photovoltaic source performances in case of degraded operating conditions for an integration feasibility in Algerian agricultural farms. Sustain Energy Technol Assess 48:101659. https://doi.org/10.1016/j.seta.2021.101659